The Astrophysical Journal, 829:53 (18pp), 2016 September 20 doi:10.3847/0004-637X/829/1/53

A GIANT LYα NEBULA IN THE CORE OF AN X-RAY CLUSTER AT $Z = 1.99$: IMPLICATIONS FOR EARLY ENERGY INJECTION

Francesco Valentino[1], Emanuele Daddi[1], Alexis Finoguenov[2,3], Veronica Strazzullo[1,4], Amandine Le Brun[1], Cristian Vignali[5,6], Frédéric Bournaud[1], Mark Dickinson[7], Alvio Renzini[8], Matthieu Béthermin[9], Anita Zanella[1], Raphaël Gobat[1,10], Andrea Cimatti[5,6], David Elbaz[1], Masato Onodera[11,12], Maurilio Pannella[1,4], Mark Sargent[13], Nobuo Arimoto[12,14], Marcella Carollo[11], and Jean-Luc Starck[1]

[1] Laboratoire AIM-Paris-Saclay, CEA/DSM-CNRS-Université Paris Diderot, Irfu/Service d'Astrophysique, CEA Saclay, Orme des Merisiers, F-91191 Gif sur Yvette, France; francesco.valentino@cea.fr
[2] Department of Physics, University of Helsinki, Gustaf Haällströmin katu 2a, 00014 Helsinki, Finland
[3] Center for Space Sciences and Technology, University of Maryland, Baltimore County, 1000 Hilltop Circle, Baltimore, MD 21250, USA
[4] Department of Physics, Ludwig-Maximilians-Universität, Scheinerstr. 1, D-81679 München, Germany
[5] Dipartimento di Fisica e Astronomia, Università degli Studi di Bologna, Viale Berti Pichat 6/2, I-40127 Bologna, Italy
[6] INAF—Osservatorio Astronomico di Bologna, Via Ranzani 1, I-40127 Bologna, Italy
[7] National Optical Astronomy Observatories, 950 N Cherry Avenue, Tucson, AZ 85719, USA
[8] INAF-Osservatorio Astronomico di Padova Vicolo dell'Osservatorio 5, I-35122 Padova, Italy
[9] European Southern Observatory, Karl-Schwarzschild-Str. 2, D-85748 Garching, Germany
[10] School of Physics, Korea Institute for Advanced Study, Hoegiro 85, Dongdaemun-gu, Seoul 02455, Korea
[11] Institute for Astronomy, ETH Zürich Wolfgang-Pauli-strasse 27, 8093 Zürich, Switzerland
[12] Subaru Telescope, National Astronomical Observatory of Japan 650 North A'ohoku Place, Hilo, HI 96720, USA
[13] Astronomy Centre, Department of Physics and Astronomy, University of Sussex, Brighton, BN1 9QH, UK
[14] Graduate University for Advanced Studies, 2-21-1 Osawa, Mitaka, Tokyo, Japan
Received 2015 November 4; revised 2016 June 10; accepted 2016 July 2; published 2016 September 21

ABSTRACT

We present the discovery of a giant $\gtrsim$100 kpc Lyα nebula detected in the core of the X-ray emitting cluster CL J1449 +0856 at $z = 1.99$ through Keck/LRIS narrow-band imaging. This detection extends the known relation between Lyα nebulae and overdense regions of the universe to the dense core of a 5–7 $\times$ 10^{13} $M_{\odot}$ cluster. The most plausible candidates to power the nebula are two *Chandra*-detected AGN host cluster members, while cooling from the X-ray phase and cosmological cold flows are disfavored primarily because of the high Lyα to X-ray luminosity ratio ($L_{\mathrm{Ly}\alpha}/L_{\mathrm{X}} \approx 0.3$, $\gtrsim$10–1000 times higher than in local cool-core clusters) and by current modeling. Given the physical conditions of the Lyα-emitting gas and the possible interplay with the X-ray phase, we argue that the Lyα nebula would be short-lived ($\lesssim$10 Myr) if not continuously replenished with cold gas at a rate of $\gtrsim$1000 $M_{\odot}$ yr^{-1}. We investigate the possibility that cluster galaxies supply the required gas through outflows and we show that their total mass outflow rate matches the replenishment necessary to sustain the nebula. This scenario directly implies the extraction of energy from galaxies and its deposition in the surrounding intracluster medium (ICM), as required to explain the thermodynamic properties of local clusters. We estimate an energy injection of the order of ≈2 keV per particle in the ICM over a 2 Gyr interval. In our baseline calculation, AGNs provide up to 85% of the injected energy and two-thirds of the mass, while the rest is supplied by supernovae-driven winds.

Key words: galaxies: active – galaxies: clusters: individual (CL J1449+0856) – galaxies: clusters: intracluster medium – galaxies: high-redshift – galaxies: star formation – Galaxy: evolution

1. INTRODUCTION

Since their first discovery in the late 1990s (Francis et al. 1996; Steidel et al. 2000), high-redshift, extended ($\gtrsim$100 kpc), and luminous (few 10^{43}–10^{44} erg s^{-1}) gas reservoirs shining by the emission of Lyα photons have progressively become a matter of debate. Despite two decades of investigation, several aspects of these "Lyα nebulae" remain puzzling, including the origin of the Lyα-emitting gas, its powering mechanism, the possible effects on the evolution of the embedded galaxies, and, ultimately, its fate (i.e., Matsuda et al. 2004; Dey et al. 2005; Geach et al. 2009; Prescott et al. 2009; Cantalupo et al. 2014). Understanding where Lyα nebulae fit in the current theoretical framework of structure formation has sparked particular interest, since they call into question a cornerstone of modern astrophysics: the complex interplay of supply, consumption, and expulsion of gas that shapes high-redshift systems. In this work, we focus on a specific feature of Lyα nebulae: the connection with their surrounding environment. This perspective complements the approaches already presented in the literature and allows us to shed light on several of the problematics listed above. First, there are observational hints that Lyα nebulae preferentially reside in overdense regions of the universe or sparse protoclusters (Steidel et al. 2000; Matsuda et al. 2004; Venemans et al. 2007). This suggests a possible connection with the formation of massive structures, even if it is not clear in which density regimes this correlation holds. Interestingly, in the local universe, the presence of kiloparsec-size, filamentary reservoirs of ionized gas in the center of "cool-core" X-ray emitting clusters (CCs) has been known for decades (Fabian et al. 1984b; Heckman et al. 1989; Hatch et al. 2007; McDonald et al. 2010; Tremblay et al. 2015). From this angle, it is tempting to view the high-redshift Lyα nebulae as the counterparts of local filaments, with sizes and luminosities reflecting the extreme conditions of the primordial universe (McDonald et al. 2010; Arrigoni-Battaia et al. 2015). However, the detailed physics of the nebular emission is still debated even for local clusters, despite the quality of the available data.

A mix of different heating mechanisms is probably at the origin of the emission by the ionized filaments, with a possible important role played by young stars formed in situ (Tremblay et al. 2015 and references therein). The origin of the cold gas has not been fully clarified either: even if modern models of auto-regulated cooling from the X-ray emitting intracluster medium (ICM) successfully reproduce several properties of the nebulae in CCs (i.e., Gaspari et al. 2012; Tremblay et al. 2015; Voit & Donahue 2015), the cold gas might also originate from a starburst event or the active galactic nuclei (AGNs) in the central brightest cluster galaxy (BCG, Hatch et al. 2007), or be uplifted by propagating radio-jets and buoyant X-ray bubbles (Churazov et al. 2001; Fabian et al. 2003), or stripped in a recent merger (Bayer-Kim et al. 2002; Wilman et al. 2006). Therefore, physical insights might not be straightforwardly gained from the simple observation of local filaments.

An attempt at assessing the validity of this suggestion can be done through the observation of giant Lyα nebulae in the core of high-redshift galaxy clusters. To date, we have lacked strong observational evidence primarily because of the scarcity of *bona fide* X-ray emitting structures discovered at $z \geqslant 1.5$ (i.e., Andreon et al. 2009; Papovich et al. 2010; Gobat et al. 2011, 2013; Stanford et al. 2012; Brodwin et al. 2015; Santos et al. 2011). Here we study in detail the case of the most distant among these X-ray detected structures, CL J1449+0856 at $z = 1.99$ (Gobat et al. 2011, 2013; Strazzullo et al. 2013, G11, G13 and S13 hereafter). Its extended emission from hot plasma and the dominant population of red, massive, and passive galaxies in the compact core (G11, G13, S13) place it in a more advanced evolutionary stage than protoclusters at similar redshift and make it a suitable candidate to start the search for nebulae in far away clusters. In this work, we present the results of a recent narrow-band imaging campaign we conducted with Keck/LRIS, with which we identified an ~100 kpc Lyα-emitting nebula in the cluster core. However, the detailed analysis of the conditions of the nebula and its environment shows some tensions with the current picture of filaments in local clusters. Even if cooling from the X-ray emitting plasma may partially contribute to the Lyα luminosity, the nebula is plausibly powered by AGNs in the cluster core.

Motivated by this discovery, we further investigate the relationship between the Lyα nebula, galaxy activity in the form of star formation and black hole growth, and the total energy content of the ICM at this early stage of the cluster evolution. The latter is a controversial issue in modern astrophysics. In fact, it has been known for more than two decades that the observed X-ray properties of the ICM in nearby clusters are inconsistent with the predictions from pure gravitational settling and an extra energy contribution is missing (Kaiser 1991; Ponman et al. 1999; Tozzi & Norman 2001). In cosmological simulations, this energy is provided by star-forming galaxies (SFGs) and AGNs through outflows, and their efficiencies can be calibrated to reproduce the properties of the local universe (e.g., Le Brun et al. 2014; Pike et al. 2014). Although the most successful models are those in which heating of the ICM happens early, such as (cosmo-) OWLS (Schaye et al. 2010; McCarthy et al. 2011), this process is still poorly constrained observationally: the timing and duration of this phenomenon, its main energy source (galactic winds from either supernovae (SNe) or AGN), and the energy transfer mechanism are subject to debate (i.e., McNamara & Nulsen 2007; Davé et al. 2008; McCarthy et al. 2011; Fabian 2012). Here we argue that the presence of the Lyα nebula is interlaced with the observed vigorous activity of galaxies in the cluster core and that it may signpost a significant energy injection into the ICM. Eventually, we estimate the amount of this injection due to strong galaxy feedback during a phase that, if prevalent in high-redshift structures, would be crucial to set the final energy budget and metal content of present-day clusters.

This paper is organized as follows. In Section 2, we present the narrow- and broadband imaging observations that led to the discovery of the Lyα nebula, along with the results of a recent *Chandra* follow-up of CL J1449+0856. In Section 3, we discuss the physical properties of the Lyα nebula, the possible powering mechanisms, and the timescales regulating its evolution, concluding that a substantial gas replenishment is necessary to feed the system. In Section 4, we focus on galaxy outflows as a plausible source of gas replenishment and we study the corresponding injection of energy into the ICM. Concluding remarks are presented in Section 5. Unless stated otherwise, we assume a ΛCDM cosmology with $\Omega_m = 0.3$, $\Omega_\Lambda = 0.7$, and $H_0 = 70$ km s^{-1} Mpc^{-1} and a Salpeter initial mass function (Salpeter 1955). All magnitudes are expressed in the AB system.

2. OBSERVATIONS AND DATA ANALYSIS

In this section, we present the Keck/LRIS narrow-band imaging of CL 1449+0856. We also describe recent *Chandra* observations, which we use to update the cluster X-ray properties previously constrained by *XMM-Newton* follow-up only. Specifically, we revise the total extended X-ray luminosity, gas temperature, and halo mass, presenting a new estimate from the velocity dispersion.

2.1. The Lyα Nebula Detection: Narrow-band Imaging

We observed CL J1449+0856 (Figure 1) for 3.5 h with the narrow-band filter NB3640 installed in the blue arm of the Keck/LRIS camera on 2014 March 27, reaching a magnitude limit of 27.1 (5σ) in an $r = 0\farcs6$ circular aperture. The average seeing during the observation was $0\farcs79$ (full width half maximum). We processed the images in a standard way with the publicly available LRIS pipeline.[15] In particular, we modeled and subtracted a super-sky image obtained as the clipped median of all the widely dithered, processed frames. We co-added individual frames weighting them by measured seeing and transparency variations during the observing night. We then combined the final narrow-band image with an aligned U-band frame from VLT/FORS2 (5σ limiting magnitude of 27.4, S13) using the formalism presented in Bunker et al. (1995) to obtain a Lyα emission map (Figures 2 and 11 in the Appendix). Color corrections are negligible, given the optimal overlap of the central effective wavelengths of the narrow- and broadband filters (3640, 3607 Å respectively). We checked the absolute flux calibration against Sloan Digital Sky Survey data, finding an agreement within 0.01 mag. We selected individual Lyα absorbers and emitters by running SExtractor in dual image mode on a χ^2 detection image and on narrow- and broadband images. We built the χ^2 detection image averaging the U and NB3640 frames weighting by their signal-to-noise ratio squared. Besides an obscured AGN (#661 in G13, see 3.3.1 below for further details), we detected only two individual bright peaks in the Lyα emission map of the cluster core (~5σ) both

[15] http://www.astro.caltech.edu/~dperley/programs/lpipe.html

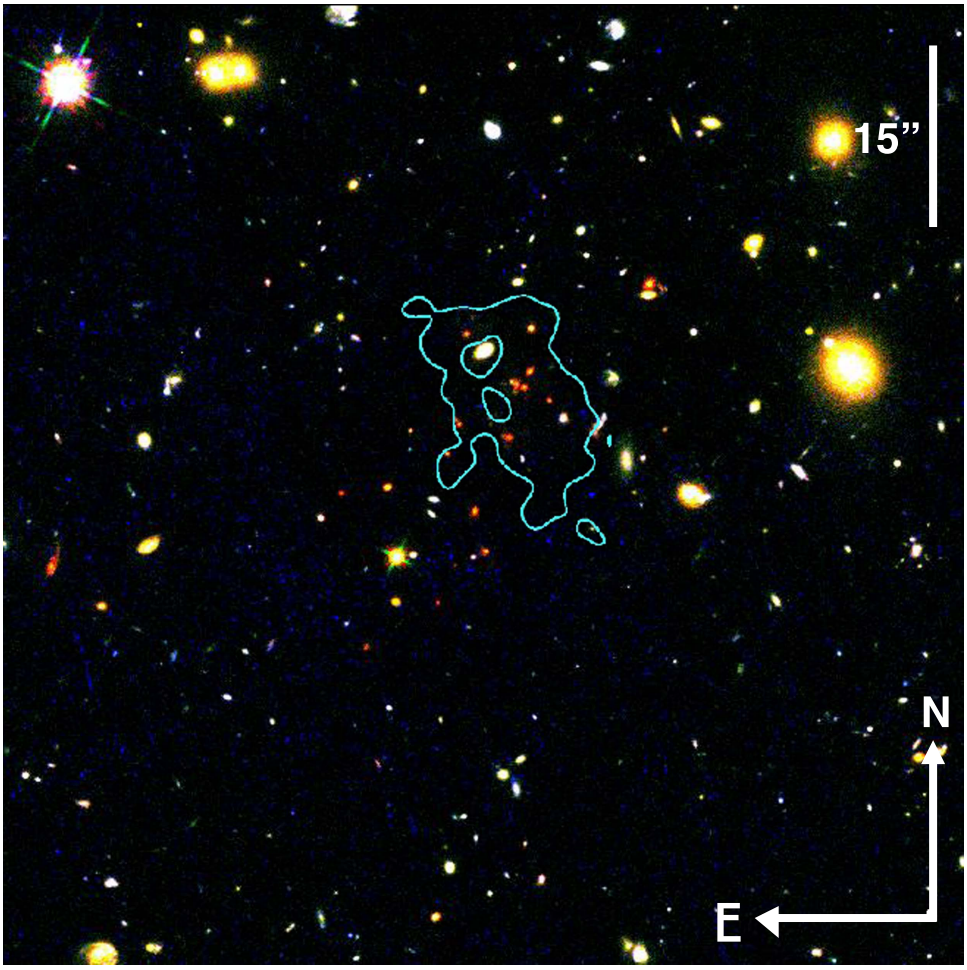

Figure 1. Cluster of galaxies CL J1449+0856 at $z = 1.99$. *HST*/F140W (red), F105W (green), and F606W (blue) RGB-composite image of CL J1449+0856. The central concentration of red galaxies represents the core of the cluster. The cyan line marks the 1σ contour of the Lyα nebula from the wavelet reconstruction.

through a classical aperture photometry approach and a wavelet analysis (Figure 3). However, they are not associated with known cluster members within a $1''$ radius in the adjacent *U* and *B* bands, nor in the deeper, but redder *Hubble Space Telescope* (*HST*)/F140W band or in the X-ray bands, suggesting that these peaks are not associated with SFGs in the cluster core. The uncertainty on the position of 5σ peaks of Lyα emission is $0\farcs07$. The bright knots may just be the densest regions of the extended Lyα nebula and the granularity (Figure 2, panel (c)) could suggest the presence of gas substructures (Cantalupo et al. 2014) or shock fronts currently beyond our detection threshold. To further confirm the detection of Lyα photons on large scales, we performed a wavelet analysis with an iterative multi-resolution thresholding and a Gaussian noise model[16] (Starck et al. 2010). The basic concept underlying wavelet decomposition is to split an image into a set of spatial frequencies, each one including the signal from sources with power on that scale. The original image is exactly recovered by adding all the “slices.” The advantage of this technique is to reduce (or remove) the impact of small-scale objects when looking for large-scale structures and its efficacy for detecting Lyα nebulae has already been shown (Prescott et al. 2012, 2013). We used this technique for the purpose of visualization (Figures 1, 2, and 11 in the Appendix) and to cross-check the results from a classical aperture photometry approach. After subtraction of the contribution from the point-like, obscured AGN (<8% of the total emission), we measure a total flux of $(8.1 \pm 1.0) \times 10^{-16}$ erg cm^{-2} s^{-1} in a ∼140 arcsec^2 polygonal aperture enclosing the whole nebula, fully consistent with the results provided by the wavelet analysis. The residual Lyα flux surrounding the AGN in the wavelet image is extended on scales larger than the point-spread function (PSF, with a full width half maximum of $0\farcs79$) and contributes to the luminosity of the nebula. We also retained the flux from the other individual bright peaks since no counterparts are detected in any other band. We estimated the 1σ uncertainty as the rms of the distribution of fluxes inside circular apertures of area equal to the one in which we measured the flux of the nebula. The total flux corresponds to an observed luminosity of $L_{\mathrm{Ly}\alpha} = (2.3 \pm 0.3) \times 10^{43}$ erg s^{-1}.

The morphology of the Lyα nebula is elongated from AGN #661 toward the center of the cluster, suggesting a physical connection (Section 3.3.1). The asymmetric shape and the miscentered location of the AGN is observed in several other nebulae at high redshift (i.e., Borisova et al. 2016) and it might simply reflect the AGN illumination cone and the gas distribution in the cluster, which naturally concentrates toward the bottom of the potential well. In fact, the peaks of the Lyα luminosity and the extended X-ray emission traced by *XMM-Newton* and *Chandra* (Section 2.3) are spatially coincident in projection, and so is the peak of the stellar mass density distribution (Figure 4), implying that the nebula effectively sits

[16] http://www.cosmostat.org/software/isap/

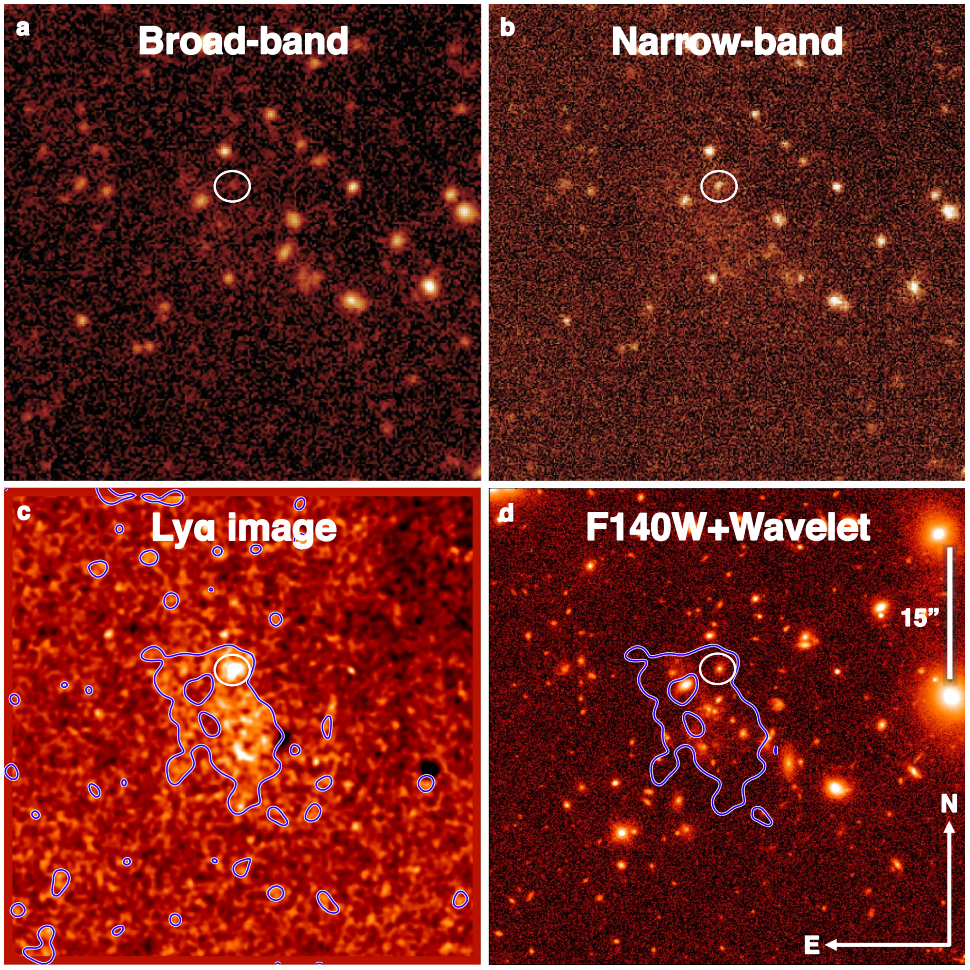

Figure 2. 100 kpc extended Lyα nebula at $z = 1.99$. Images of CL J1449+0856 in the broad U band (panel (a)) and NB3640 narrow-band (panel (b)), and a continuum-subtracted Lyα emission line map smoothed on scales of 1″ (panel (c)). The white circle indicates the heavily obscured AGN #661 (G13). The extended emission southward is the Lyα nebula. Panel (d) shows the *HST*/WFC3 F140W image. In panels (c) and (d), the blue line marks the 1σ contour of the large-scale Lyα emission from the wavelet reconstruction after the subtraction of point-like sources. For reference, 15″ correspond to ~125 kpc at $z = 1.99$.

in the cluster core. Note that the peaks mapped by *XMM-Newton* and *Chandra* are consistent within the positional uncertainties (16″ and 4″ respectively). In Figure 5, we show the radial profile of the Lyα surface brightness and the projected stellar mass density. For both profiles, we fixed the same center at the peak of the projected stellar mass density distribution. Moreover, we merged the measurements at the two farthest positions from the cluster center to increase the signal, and we subtracted the contribution of AGN #661. As opposed to the stellar component that traces the cluster potential well, the Lyα surface brightness profile appears flat over the whole extension of the nebula. A drop is expected to occur at some radius, but Figure 5 suggests that this happens at larger scales than for the stellar component.

2.2. Extended Continuum Emission

We measured the continuum emission associated with the Lyα nebula from a pure "continuum emission map" (Bunker et al. 1995) and both *Subaru*/Suprime-Cam B (G11) and Keck/LRIS V-band imaging. We do not expect strong emission lines from sources at $z = 2$ to fall in the observed B and V bands. These frames are, respectively, 2.5 times and 3.3 times deeper than the continuum image and provide a better constraint on the Lyα equivalent width of the nebula (EW(Lyα)). In unobscured SFGs, the flux density F_ν is roughly constant at wavelengths bluer than 2000 Å, and thus possible color biases in the evaluation of the EW(Lyα) using B- and V-band continua are limited. We measured the continuum emission only where we detected the extended Lyα emission at more than a 5σ significance (Figure 11 in the Appendix, panel (d)). Evident B- and V-band sources were masked so as not to contaminate the diffuse emission. We did not individually detect a significant integrated continuum emission in any of the frames. Assuming a constant F_ν and combining the three bands, we estimated an average continuum emission of $(3.38 \pm 0.95) \times 10^{-19}$ erg cm^{-2} s^{-1} angstrom^{-1} and a corresponding Lyα equivalent width of EW(Lyα) $= 271^{+107}_{-60}$ Å, compatible with the 2σ lower limit we derived from the sole continuum image (EW(Lyα) > 192 Å). We note here that the 3σ detection is formally reached only by including the V band, which could contain residual contaminating emission from red passive galaxies. Thus, it would be appropriate to regard the quoted EW measurement as a lower limit.

2.3. Chandra X-Ray observations

CL J1449+0856 has been imaged both with *XMM-Newton* (80 ks, G11, Brusa et al. 2005) and *Chandra* (94 ks, Campisi et al. 2009). Details of the *XMM-Newton* detection have already been reported in G11. However, that analysis suffered from a

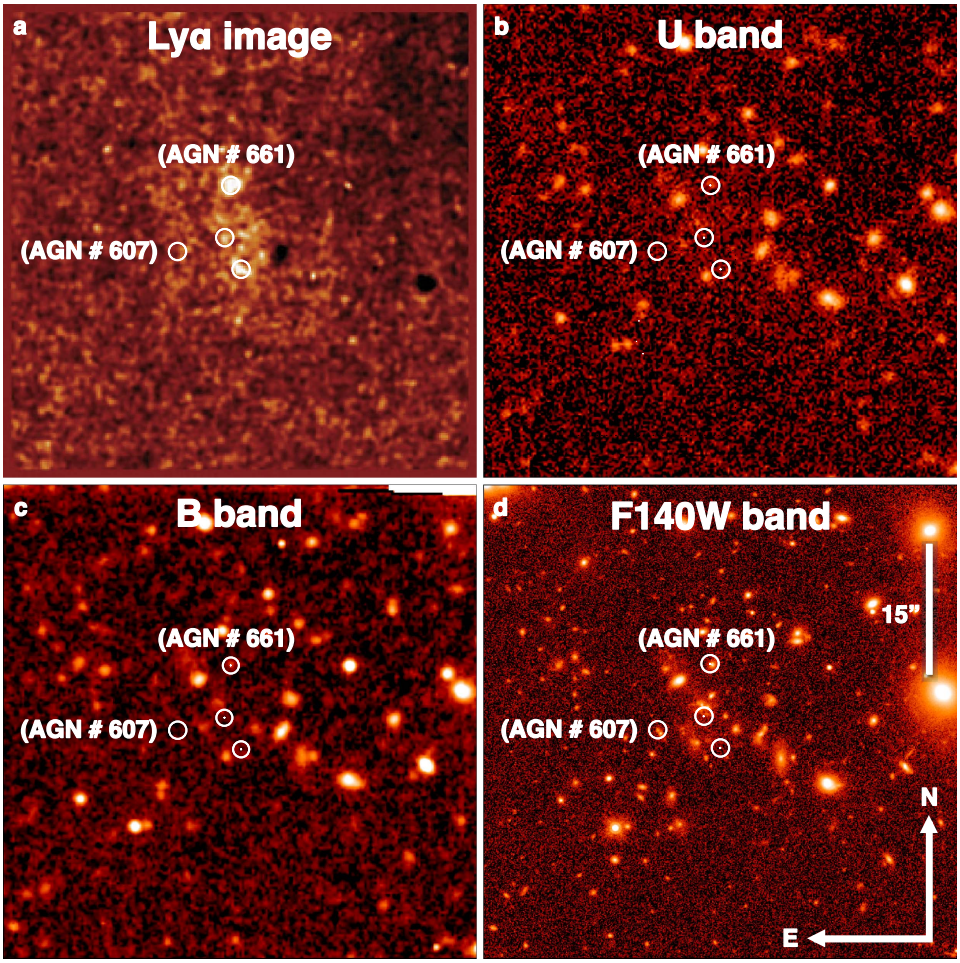

Figure 3. Bright knots in the Lyα nebula. Lyα emission line map smoothed over a 1″ area (panel (a)) and *U*-band (panel (b)), *B*-band (panel (c)), and F140W band (panel (d)) images of CL J1449+0856. Individual Lyα emitters detected at $\sim 5\sigma$ are marked (white circles). The position of the AGN # 607 is reported for clarity, but this source is not identified as a Lyα emitter. For reference, 15″ corresponds to ~125 kpc at $z = 1.99$.

large uncertainty on the localization of the cluster center. Based on the statistical analysis of galaxy groups in COSMOS (George et al. 2011), the difference between the most massive members and the X-ray peak positions is typically 15″ (Figure 4, panel (b)). The measured distance between the core of the cluster and the XMM position is 9″.

Archival ACIS-I *Chandra* observations of the field consist of a mosaic of three partially overlapping pointings of ≈30 ks each, covering a total area of ≈500 arcmin^2 at different depths. These three observations (5032, 5033, and 5034) were performed in 2004 June by the Advanced CCD Imaging Spectrometer (ACIS) with the I0 CCD at the aimpoint and all ACIS-I CCDs in use. Faint mode was used for the event telemetry, and ASCA grade 0, 2, 3, 4, and 6 events were used in the analysis (full details are reported in Campisi et al. 2009). In Cycle 16, we followed-up the field with the ACIS-S camera (aimpoint at CCD = 7) for a nominal exposure of 94.81 ks in very faint mode. This new *Chandra* observation has a higher spatial resolution because it is pointed at the location of the diffuse emission and, thus, improves the localization of the cluster core and the association between the extended X-ray source and the optical/near-IR counterpart. For both ACIS-I and ACIS-S data, reprocessing was carried out using CIAO version 4.6 and adopting the latest relevant calibration products. From a wavelet reconstruction of the ACIS-S image, we detected a $>4\sigma$ extended feature co-aligned with the core (Figure 4, panel (a)). The X-ray source is centered on coordinates 14:49:13.670, +8:56:28.25 with a 1σ uncertainty on the position of 4″ (Figure 4, panel (b)) and a distance to the cluster core of 5″. We measured the extended source flux in the area where the significance of the wavelet map was higher than 2σ. We derived ACIS-S and ACIS-I counts independently, using the same extraction region. Within a 10″ aperture, the net (i.e., background-subtracted) number of counts from the extended source in ACIS-S is 11.0 ± 5.3 (94 ks exposure) in the 0.5–2 keV band, corresponding to an aperture flux of $(8.5 \pm 3.0) \times 10^{-16}$ erg cm^{-2} s^{-1}. The ACIS-I counts and aperture flux are 5.2 ± 2.5 and 1.2×10^{-15} erg cm^{-2} s^{-1} respectively (49 ks exposure). The average flux of the source is therefore $(1.0 \pm 0.4) \times 10^{-15}$ erg cm^{-2} s^{-1}. This corresponds to an observed total X-ray luminosity of $L_X = (9 \pm 3) \times 10^{43}$ erg s^{-1} in the 0.1–2.4 keV rest-frame band within R_{500}, defined as the radius enclosing a mean overdensity 500 times larger than the critical density of the universe. We do not detect bright radio sources close to the cluster core in deep Jansky Very Large Array observations at 3 GHz down to 2.7 μJy (rms), except for two galaxies with a ~30 μJy continuum emission, fully consistent with pure star formation activity seen at ultra-violet and infrared wavelengths. Thus, inverse Compton scattering off extended radio-galaxy jets is not likely to be the origin of the extended X-ray emission as in potentially similar cases (i.e., Miley et al. 2006).

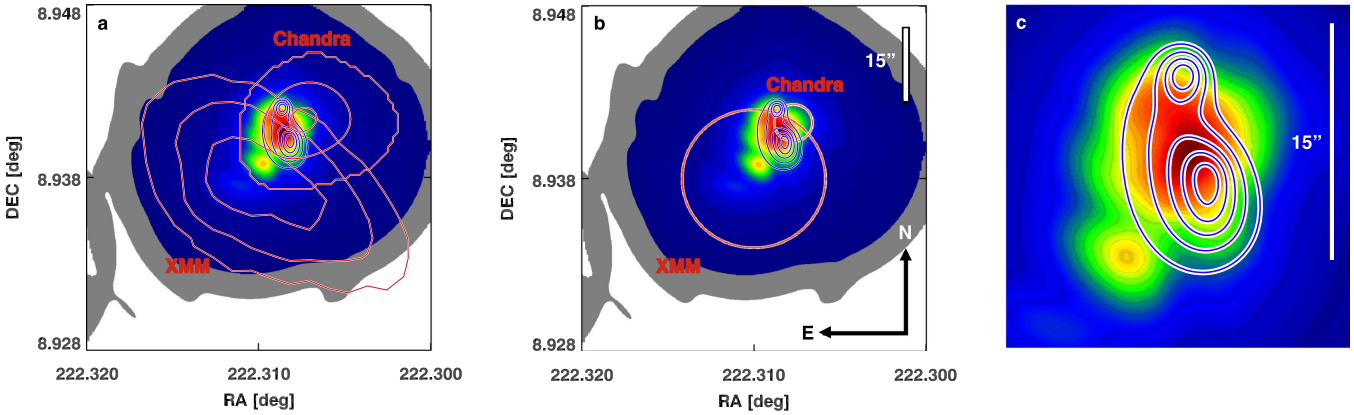

Figure 4. Spatial distributions of stellar mass density, Lyα surface brightness, and X-ray extended emission. Stellar density maps are derived from a mass complete sample of cluster members and candidates with $M_\star \geqslant 10^{10.4}\ M_\odot$ (S13, background colored image in panels (a)–(c)). The prominent stellar mass density peak represents the cluster core region (red area). Lyα nebula $\geqslant 3\sigma$ contours from wavelet reconstruction are superimposed (blue lines). Note that point-like sources have been subtracted before tracing the contours. Extended X-ray contours from *XMM-Newton* and *Chandra* observations (red lines) are displayed in panel (a). The positional uncertainties of the peak of the X-ray extended emission from both sets of observations are shown in panel (b) (red circles). A zoom on the central region is shown in panel (c). For reference, 15″ corresponds to ∼125 kpc at $z = 1.99$.

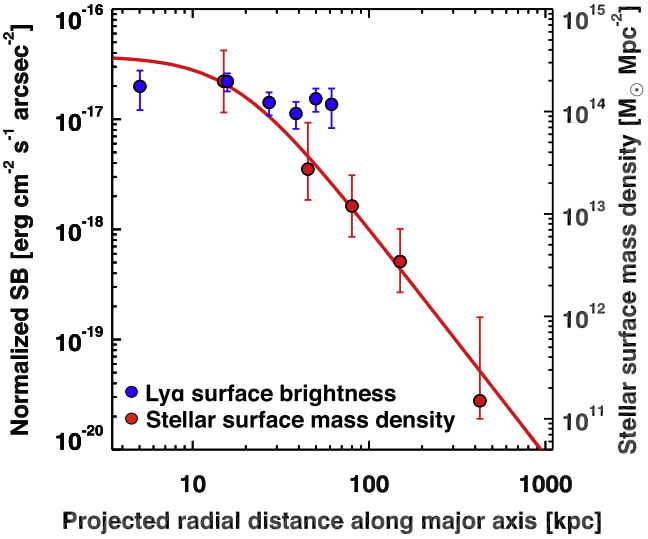

Figure 5. Lyα nebula and projected stellar mass density profiles. We show the stellar mass density (red circles) and normalized Lyα surface brightness (blue circles) radial profiles. The center of the profiles are spatially coincident and fixed at the position of the barycenter of stellar mass (S13). For the Lyα surface brightness profile, we merged the measurements at the two farthest positions from the cluster center to reach the formal detection threshold. Moreover, the Lyα flux of AGN #661 has been subtracted in the corresponding bin. For the stellar mass density profile, error bars include both the Poisson error and the uncertainties in membership determination (S13). For the surface brightness profile, error bars represent the 1σ uncertainties on flux measurements. The best fit of the stellar mass profile is a classical beta-model (S13).

2.4. Halo Mass and Gas Temperature

Scaling the observed total X-ray luminosity within R_{500} (Leauthaud et al. 2010), we estimated a halo virial mass of $M_{\rm halo} = (5\text{–}7) \times 10^{13}\ M_\odot$ and a virial radius of $R_{\rm vir} = 0.5 \pm 0.1$ Mpc, in agreement with previous determinations (G11, G13). This estimate is consistent with that expected from a total stellar mass enclosed in cluster members of $2 \times 10^{12}\ M_\odot$, in particular, in six massive and passive galaxies in the core (S13, $M_{\rm halo} = 4\text{–}7 \times 10^{13}\ M_\odot$, including the latest calibration by van der Burg et al. 2014). We independently evaluated $M_{\rm halo}$ from the velocity dispersion derived from *HST*/WFC3 and *Subaru*/MOIRCS spectroscopy (G13, Valentino et al. 2015). After excluding obvious interlopers at redshift $z < 1.95$ and $z > 2.05$, we estimated the systemic redshift and the velocity dispersion fixing the reduced $\chi^2_{\rm red} = \left(\sum_{i=1}^{N}(z_{\rm i} - z_{\rm sys})^2/(\sigma^2_{z_{\rm i}} + \sigma^2_{\rm disp})\right)/{\rm dof} = 1$, applying a clipping at 3σ, and iterating until convergence. This procedure allows us to fully take into account the uncertainties on spectroscopic redshifts. We then estimated the uncertainties as the 15.87–84.13 percentile ranges of the distribution of 15,000 bootstrap simulations. We obtain $z_{\rm sys} = 1.995^{+0.003}_{-0.004}$ and $\sigma_{\rm vel} = (830 \pm 230)$ km s^{-1}. We find consistent results modeling a Gaussian curve on the galaxy redshift distribution (Figure 6). Assuming virialization, we find a 1σ lower limit on the virial mass of $M_{\rm halo} \gtrsim 4 \times 10^{13}\ M_\odot$ obtained adopting the 1σ lower limit on $\sigma_{\rm vel}$. Then, we calculated a total intracluster mass in the hot phase of $M_{\rm ICM} \approx 0.08 \times M_{\rm halo} \approx 5 \times 10^{12}\ M_\odot$ (Renzini & Andreon 2014). The gas fraction may vary with redshift, but even considering a value close to the universal baryon fraction, the main result of this work would not change. Assuming spherical geometry for the halo and a mean molecular weight of $\mu = 0.6$, the average particle density is $(8 \pm 2) \times 10^{-4}$ cm^{-3} within the virial radius. Finally, we estimated a temperature of 2.1 keV from the $L_{\rm X} - T$ relation (Finoguenov et al. 2007) and an absorbing column density of $N_{\rm H} = 2 \times 10^{20}$ cm^{-2}. We stress here that the current X-ray data set allows only for an estimate of the integrated X-ray luminosity $L_{\rm X}$. We do not have in-hand the spatial profiles of X-ray derived quantities such as the temperature, entropy, density, or the metallicity of the hot ICM. In order to estimate these physical quantities, we rely on the extrapolation of well established relations at low and moderate redshift ($z < 1$).

3. PHYSICS OF THE LYα NEBULA

In this section, we study the physics of the Lyα nebula. First, we estimate the mass and electron density from its luminosity and size. We then explore the possible powering mechanisms and conclude that the most plausible source of ionizing photons are AGNs embedded in the nebula, with a possible contribution from dissipation of the mechanical energy due to galaxy outflows. Finally, we discuss the typical timescales regulating the evolution of the nebula. We find that, barring an observational coincidence, in our favored scenario the nebula

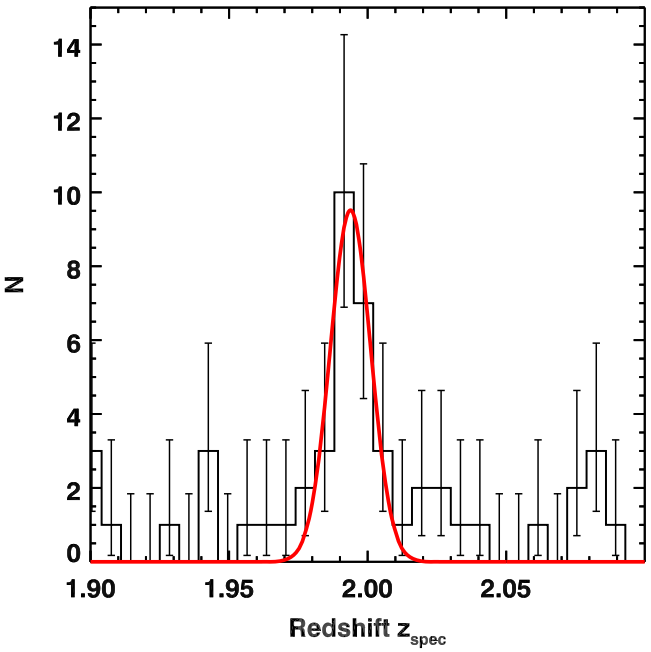

Figure 6. Cluster redshift distribution. The black histogram shows the redshift distribution of galaxies in CL J1449+0856. The red curve is the best Gaussian model fitting the curve. The uncertainties represent the formal 68.3% Poisson confidence interval.

is constantly replenished with cold gas to survive evaporation due to the surrounding hot X-ray plasma.

3.1. Mass and Density

Assuming photoionization, we can estimate the mass $M_{\mathrm{Ly}\alpha}$ and the electron density n_{e} of the ionized gas from the Lyα luminosity (McCarthy et al. 1990; Dey et al. 2005):

$$M_{\mathrm{Ly}\alpha} = 1.25\, m_{\mathrm{p}}\, n_{\mathrm{e}} f\, V = (1 - 10) \times 10^{9}\, M_{\odot} \quad (1)$$

where m_{p} is the proton mass, f the volume filling factor, and V the volume of the nebula. For the sake of simplicity, we assumed a spherical geometry for the nebula with a radius of $R_{\mathrm{neb}} = 46$ kpc, the average value of the long and short axes measured in the wavelet reconstructed image. The choice of the shape does not affect the final result of this work, i.e., adopting a cylindrical symmetry the volume changes by ≈10%. We assumed $f = 10^{-3}$–10^{-5} as detailed in the next section. The electron density is derived from the Lyα luminosity estimate through

$$L_{\mathrm{Ly}\alpha} = \frac{j_{\mathrm{Ly}\alpha}}{j_{\mathrm{H}\beta}}\, \alpha^{\mathrm{eff}}_{\mathrm{H}\beta}\, h\nu_{\mathrm{H}\beta} n_{\mathrm{e}}\, n_{\mathrm{p}} f\, V \rightarrow n_{\mathrm{e}} = 0.9 - 9\ \mathrm{cm}^{-3}, \quad (2)$$

where $j_{\mathrm{Ly}\alpha}$ and $j_{\mathrm{H}\beta}$ are the emission coefficients for Lyα and Hβ, $\alpha^{\mathrm{eff}}_{\mathrm{H}\beta}$ is the effective recombination coefficient for Hβ, $h\nu_{\mathrm{H}\beta}$ is the energy of an Hβ photon, and n_{p} is the proton number density ($n_{\mathrm{e}} \approx 1.2\, n_{\mathrm{p}}$ accounting for doubly ionized helium). The range of n_{e} values corresponds to $f = 10^{-3}$–10^{-5}, assuming case B recombination (Osterbrock & Ferland 2006) and $T = 10^{4}$ K. We notice that the gas appears marginally optically thick to ionizing radiation, given the column density of neutral hydrogen averaged over the projected area of the nebula of $\langle N_{\mathrm{H\,I}} \rangle \approx 10^{17.2}$ cm^{-2} (see Equation 11 in Hennawi & Prochaska 2013). Moreover, $n_{\mathrm{e}} \propto (\sqrt{f})^{-1}$ and $M_{\mathrm{Ly}\alpha} \propto \sqrt{f}$, reducing the two orders of magnitude range of uncertainty that we allowed for f. Finally, $M_{\mathrm{Ly}\alpha}$ might be a lower limit for the total mass of cold gas reservoirs in the cluster if AGNs are the powering sources (see Section 3.3), as beamed emission may illuminate only a portion of the gas. In addition, the true Lyα luminosity may be higher than reported due to dust and neutral hydrogen absorption.

3.2. Volume Filling Factor

The mass and density of the nebula depend on the volume filling factor f, which is not directly constrained by our observations. However, it is reasonable to assume pressure equilibrium between the ionized gas and the hot X-ray ICM, allowing us to put an upper limit on the possible values of f. To estimate the pressure exerted by the hot ICM, we assumed the universal pressure profile of galaxy clusters (Arnaud et al. 2010), properly rescaled in mass and redshift, as representative for CL J1449+0856. Then, dividing the pressure by $\sim 10^{4}$ K, the typical temperature of the Lyα gas, we obtained the radial density profile of a medium in pressure equilibrium with the X-ray emitting plasma. The range of possible values of n_{e} over the radial extension of the nebula is $n_{\mathrm{e}} \sim 1$–10 cm^{-3}, corresponding to $f \sim 10^{-3}$–10^{-5}, a pressure of $p \sim 10^{4}$–10^{5} K cm^{-3}, and masses of ionized gas of $M_{\mathrm{Ly}\alpha} \sim (1 - 10) \times 10^{9} M_{\odot}$. Absent an observed X-ray profile, this is an order of magnitude calculation, given that the pressure profile in low-mass systems might be different and, notably, flatter than in clusters (Le Brun et al. 2015), leaving the door open for larger values of f and lower densities. However, higher values of f (∼0.01–1) are disfavored by a simple argument based on gravitational stability: if larger and more massive clouds were in place, they would be Jeans-unstable and form new stars, a scenario disfavored by the observed high value of EW(Lyα) (Section 3.3.2). On the contrary, solutions with $f \lesssim 10^{-3}$ are gravitationally stable, considering the simplified case of auto-gravitating spheres of stably ionized gas at 10^{4} K.

On the other hand, much smaller values of f are not easily maintained for long timescales. As recognized in classical works (Fabian et al. 1987; Crawford & Fabian 1989), lower volume filling factors and higher densities would imply clouds dissipating by thermal expansion on short timescales (10^{5} years), with consequent difficulties to explain the size of the nebula and its lifetime.

3.3. Powering Mechanism and Origin of the Gas

We consider five different physical scenarios to explain the extended Lyα emission: hard ionizing spectra of AGNs impacting gas reservoirs in the cluster core, the continuous formation of young massive stars, cooling of dense cosmological cold flows penetrating into the dark matter halo, cooling of plasma from the X-ray phase, and dissipation of the mechanical energy from galaxy outflows in the core. Eventually, we point to the AGN radiation field as the most plausible powering source of the Lyα nebula, with a potential contribution from shocks induced by galaxy outflows.

3.3.1. AGNs in the Cluster Core

Two spectroscopically confirmed X-ray AGNs in the cluster core (#607, 661 in G13) are suitable candidates for ionizing the nebula. The depth of the new *Chandra* observation, coupled with an optimal on-axis alignment, allowed us to perform a basic X-ray

spectral analysis despite the limited photon statistics (34 and 20 net counts in the observed 0.5–7 keV band for sources #607 and 661, respectively). Source #607 is characterized by a power-law spectrum with photon index $\Gamma = 2.0 \pm 0.6$; the observed 2–10 keV flux is $1.7^{+1.1}_{-0.6} \times 10^{-15}$ erg cm^{-2} s^{-1}, corresponding to a rest-frame 2–10 keV luminosity of $5.2^{+3.4}_{-1.8} \times 10^{43}$ erg s^{-1}, typical of a luminous Seyfert galaxy. The X-ray spectrum of source #661, the point-like Lyα emitter (Figure 2), is flat: fitting the data with a power-law model provides $\Gamma = -0.7^{+0.8}_{-0.9}$, highly indicative of strong obscuration. We then included an absorption component and fixed the photon index to 1.8, as expected for the intrinsic AGN emission (e.g., Piconcelli et al. 2005). This model results in a column density of $N_{\rm H} = 9.3^{+5.6}_{-4.0} \times 10^{23}$ cm^{-2}, i.e., consistent with marginal Compton-thick absorption (1.5×10^{24} cm^{-2}). The tentative detection of an iron Kα emission line at 6.4 keV (with equivalent width of $\approx$2.4 keV rest frame), if confirmed, would further support the heavily obscured nature of source #661. The derived 2–10 keV flux is $(7.4 \pm 2.2) \times 10^{-15}$ erg cm^{-2} s^{-1}, corresponding to a rest-frame luminosity of $L_{2-10\,\rm keV} = 2.9^{+0.6}_{-0.5} \times 10^{44}$ erg s^{-1}, placing source #661 in the quasar regime. We do not detect any bright counterpart in deep Jansky Very Large Array observations at 3 GHz down to 2.7 μJy (rms), and we thus classify source #661 as radio-quiet. From aperture photometry, we estimated a Lyα flux of $(6.7 \pm 0.7) \times 10^{-17}$ erg cm^{-2} s^{-1}, corresponding to a luminosity of $(1.9 \pm 0.2) \times 10^{42}$ erg s^{-1}. The spectral energy distribution (SED) of #661 is shown in Figure 7. From SED modeling, which benefits from near-, mid-, and far-IR observations from *Spitzer* and *Herschel*, we estimated a bolometric luminosity for the AGN of $(2.7 \pm 1.5) \times 10^{45}$ erg s^{-1}. A similar value ($3.2 \pm 0.6 \times 10^{45}$ erg s^{-1}) is derived using the observed [O III]λ5007 Å luminosity obtained from recent *Subaru*/MOIRCS spectroscopy of the galaxy (Valentino et al. 2015), converted into a bolometric luminosity as $L_{\rm bol}/L_{\rm [O\,III]} = 3500$ (Heckman et al. 2004). Assuming the luminosity-dependent bolometric correction as in Lusso et al. (2012), we predict an intrinsic 2–10 keV luminosity for source #661 of $1.6^{+1.6}_{-0.5} \times 10^{44}$ erg s^{-1}. This value is consistent, within the uncertainties due to the adopted relations and measurements, with that derived from the X-ray spectral analysis reported above.

Furthermore, we normalized the "radio-quiet AGN" template by Elvis et al. (1994) to match the estimated $L_{\rm bol}$. We then integrated over wavelengths bluer than the Lyman continuum limit to obtain the ionizing photon flux ϕ from both sources. We obtained $\phi \sim 1.3 \times 10^{55}$ and $\phi \sim 7.3 \times 10^{54}$ photons s^{-1} for source #661 and #607, respectively. Taking into account the distance between the AGN and the peak of diffuse Lyα emission, a conical illumination pattern of the neutral gas, and a covering factor of the ionized gas $f_{\rm C} \sim 1$ consistent with the observations (Section 3.5), we estimate that (6.5–15.3)% and (14.5–49.2)% of ionizing photons from #661 and #607 reach and ionize the gas. The number of ionizing photons necessary to explain the observed Lyα luminosity is

$$\phi = \frac{L_{\rm Ly\alpha}}{h\,\nu_{\rm Ly\alpha}} \frac{1}{\xi_{\rm Ly\alpha}} \approx 1.8 \times 10^{54}\ \text{photons s}^{-1} \qquad (3)$$

where $\xi_{\rm Ly\alpha} = 0.68$ is the fraction of ionizing photons converted in Lyα (Spitzer 1978). Thus, the AGNs are likely capable of producing a sufficient amount of ionizing radiation to power the gas emission, even if $f_{\rm C}$ were a factor of several times smaller. We note that the flat Lyα surface brightness distribution in Figure 5 is not a priori in contradiction with powering from the AGN. The geometry of the system, the absorbing torus around the AGN, and the distribution of the cold clouds impact the observed profile: the flatness might just reflect covering factors close to unity. In fact, for volume filling factors $f = 10^{-3}$–10^{-5} and a covering factor $f_{\rm C} \sim 1$, energetic photons from the AGN may ionize gas at large distances. Finally, we note that resonant pure scattering of Lyα photons from #661 can hardly contribute to the diffuse luminosity farther than ~10 kpc—less than 10% of the whole extension of the nebula—as detailed radiative transfer modeling shows (Cantalupo et al. 2005; Dijkstra et al. 2006).

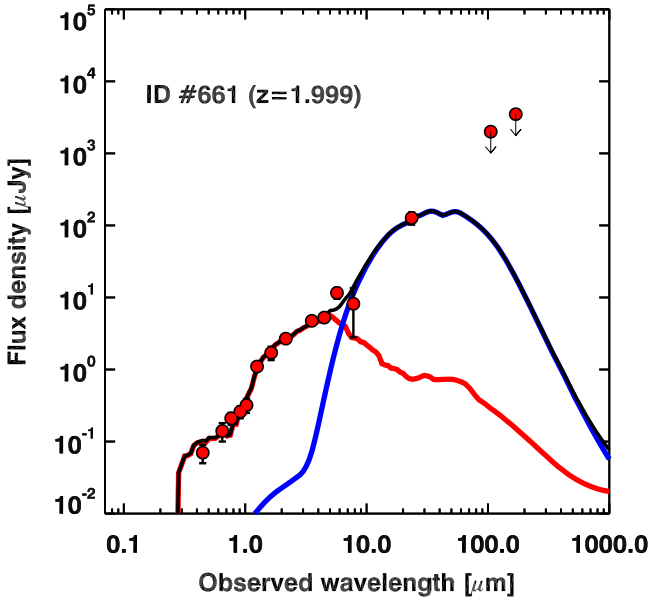

Figure 7. SED modeling of the marginally Compton-thick AGN #661. *U*-band to *Herschel*/SPIRE 250 μm observations are shown (red circles). The contributions of stars (red line) and the AGN (blue line) are shown independently. The full model is the sum of the two components (black line). The spectroscopic redshift is from *Subaru*/MOIRCS (Valentino et al. 2015).

3.3.2. Young Massive Stars

Ongoing and continuous formation of young stars spread over the nebula might be a possible alternative ionizing source (Miley et al. 2006). The total star formation rate (SFR) inferred from the Lyα luminosity is $21 \pm 3\ M_{\odot}$ yr^{-1} (Kennicutt 1998), assuming an intrinsic ratio of $L_{\rm Ly\alpha}/L_{\rm H\alpha} = 8.7$ (Case B recombination, Osterbrock & Ferland 2006). This estimate should be regarded as a strong lower limit on the total SFR since we do not correct $L_{\rm Ly\alpha}$ for dust obscuration and scattering from neutral hydrogen. However, both truly diffuse star formation and the emergence of undetected galaxies populating the low-mass end of the mass function and contributing to the diffuse emission (Zibetti et al. 2005) are disfavored: the high value of EW(Lyα) $= 271^{+107}_{-60}$ Å implies ages too young to be reasonably observable (Section 2.2 and Figure 7 in Schaerer 2003). Assuming a continuous star formation history, we should observe stars younger than $\lesssim$3 Myr distributed over a 100 kpc scale, much larger than the typical super-star cluster size. For comparison, EW(Lyα) is ~100 Å for the continuous star formation regime. A single, simultaneous starburst event on the same scale seems even less likely. Small effects due to the choice of the initial mass function or metallicity do not

change these results, unless considering extreme Population III stars (Schaerer 2003). We stress here that the weak continuum detection is formally reached only by averaging the U frame with redder bands, which could contain residual contaminating emission from red passive galaxies. In addition, the Lyα flux is not corrected for dust absorption and scattering from neutral hydrogen. Hence, the quoted EW measurement is reasonably a lower limit of the true value.

3.3.3. Cosmological Cold Flows

Another viable origin for the Lyα photons is the cooling of the dense streams penetrating into dark matter halos currently predicted by hydrodynamical cosmological simulations (Dekel et al. 2009; Goerdt et al. 2010). The current status of these models disfavors this scenario showing that, given the halo mass of CL J1449+0856, these cold flows should have stopped reaching the cluster core ~1 Gyr prior to observation, being shock-heated to the virial temperature (Valentino et al. 2015). Nevertheless, in the cluster core, we estimate a total SFR of $\approx$1000 $M_{\odot}$ yr^{-1} (Section 4.1) that must be constantly fueled by fresh cold gas given the 0.5 Gyr gas depletion timescale typical at $z = 2$ (Daddi et al. 2010; Tacconi et al. 2013). This points to an inconsistency with the prescriptions of present-day models. Note, however, that the mass and redshift regimes at which cold flows should not penetrate into the hot ICM have not been observationally confirmed yet, and suffer from substantial scatter in simulations (Dekel et al. 2009). In addition, there are hints that within this scatter a cluster progenitor at $z = 2$ may be crossed by dense gas streams supporting high SFRs and powering extended Lyα nebulae (Danovich et al. 2015). For the rest of the paper, we will adopt the predictions of current cosmological simulations, excluding a substantial contribution to the Lyα luminosity from cold flows. We defer a more detailed discussion to future work.

3.3.4. Classical Cooling Flows and Cool-cores

Cooling from the X-ray emitting phase to a cold ~10^4 K temperature is known to occur at low redshift and is generally considered the origin of the nebular filaments observed in cool-core clusters (CCs, Fabian et al. 1984b; Heckman et al. 1989; Hatch et al. 2007; McDonald et al. 2010; Tremblay et al. 2015). More extreme manifestations of the same mechanism are the classical cooling flows, though obvious cases are not currently known in the local universe (Peterson & Fabian 2006). Even though we cannot properly classify CL J1449+0856 as CC or non-CC according to the standard X-ray based definition owing to poor X-ray sensitivity at $z = 2$, we find several inconsistencies between this cluster and the typical local CCs or classical cooling flows. First, the ratio between the *Ly*α luminosity of the nebula and the total X-ray luminosity of the ICM is orders of magnitude larger in CL J1449+0856 than predicted for classical cooling flows or observed in local CCs. In CL J1449+0856, we find $L_{\rm Ly\alpha}/L_{\rm X} \sim 0.3$, while $L_{\rm Ly\alpha}/L_{\rm X} \sim 10^{-3}$ and $\sim 0.5 \times 10^{-3}$ for classical stationary cooling flows (Cowie et al. 1980; Bower et al. 2004; Geach et al. 2009) and CCs, respectively. To compute the ratio for local CCs, we collected measurements of extended Hα luminosities from the survey by McDonald et al. (2010) and the X-ray flux observed with *ROSAT* (Ledlow et al. 2003). Assuming $L_{\rm Ly\alpha}/L_{\rm H\alpha} = 8.7$ (Case B recombination, Osterbrock & Ferland 2006), we derived an average $L_{\rm Ly\alpha}/L_{\rm X}$ ratio of 5×10^{-4} (40% less when including only the extended filaments and not the flux from the BCG) for 13 structures in the Abell catalog. This is a conservative upper limit, since our Lyα measurement for CL J1449+0856 is not corrected for reddening nor scattering. The only cases when $L_{\rm Ly\alpha}/L_{\rm X} \sim 0.01$ happen in the presence of strong radio-galaxies (i.e., Hydra A), while we exclude the presence of such sources in CL J449+0856 thanks to our deep JVLA 3 GHz maps down to 2.7 μJy (rms). This was already recognized in the seminal paper by Heckman et al. (1989) where the highest $L_{\rm Ly\alpha}/L_{\rm X}$ ratios strongly correlate with the presence of a bright radio-galaxy in the core (Cygnus A, 3C 295, Perseus) and consequently show high excitation lines in the spectra of the nebulae. For reference, the widely studied case of the Perseus cluster (i.e., Fabian et al. 1984a; Conselice et al. 2001; Hatch et al. 2005, 2007) shows $L_{\rm Ly\alpha}/L_{\rm X} \lesssim 5 \times 10^{-3}$. We stress once more that we do not measure a proper observed X-ray profile for the cluster. Thus we cannot isolate the core luminosity (better correlated with the nebular luminosities, Figures 9 and 11 in Heckman et al. 1989), but we can only compare global properties (their Figure 10). Overall, the Lyα nebula we discovered is hugely overluminous with respect to local analogs: only $\ll$1% of its luminosity could be explained if CL J1449+0856 were the high-redshift version of a typical low-redshift CC.

Moreover, local nebular filaments are frequently connected with episodes of star formation. If not in the filaments themselves—observationally there is not clear evidence disproving this possibility (McDonald et al. 2010; O'Dea et al. 2010; Tremblay et al. 2015)—star formation should occur at least in the central galaxies, fueled by the gas cooled from the X-ray phase. The presence of large molecular gas reservoirs associated with the filaments (Salomé et al. 2011; McNamara et al. 2014) further supports this argument. In CL J1449+0856 this is not observed: the peak of the extended Lyα emission (once the contribution of the offset point-like AGN has been removed) does not overlap with any cluster member, nor to any evident source in all bands from U to near-infrared *HST*/F140W. In this sense, if cooled gas is flowing toward the bottom of the potential well where the peak of the Lyα emission lies (Figure 4), it is not triggering star formation nor AGN feedback in any object.

Finally, as we will show later in Section 4.2, SFGs and AGNs in the cluster core can inject a huge amount of energy into the surrounding medium. Considering only mechanical energy, this quantity is five times higher than the observed X-ray luminosity at $z = 1.99$, largely enough to offset *global* catastrophic cooling from the ICM and to strongly disfavor the hypothesis of a classical cooling flow. However, *local* rapid cooling may arise at the peak of the density distributions in the ICM, caused by the onset of thermal instabilities. This argument is at the base of modern feedback regulated models of ICM cooling, which have proved to successfully reproduce several properties of the local nebular filaments (Gaspari et al. 2012; Sharma et al. 2012). Here we cannot directly test the simple prescription proposed in these models based on the ratio between the free-fall time and the timescale necessary to start the thermal instabilities. Nevertheless, we note that feedback is likely to play a role (Section 4.2), even if a circular "on-off" auto-regulated regime might not be easily established at high redshift, given the long gas depletion timescales in galaxies (0.5–1 Gyr, Daddi et al. 2010; Tacconi et al. 2013) compared with the age of the universe.

We conclude that the observed Lyα emission is not due to cooling from the X-ray phase in the form of a classical stationary flow. On the other hand, if moderate cooling partially contributes to the total Lyα luminosity regulated by feedback, it generates very peculiar features not observed in local CCs.

3.4. Shocks

Lyα emission could be powered by shocks induced by galaxy outflows on the surrounding pressurized ICM. We constrain the maximum fraction of total kinetic energy injected by winds that is lost by radiative losses simply dividing the total power radiated through emission lines ($\approx$2 times the observed total Lyα luminosity $L_{\mathrm{Ly}\alpha}$) by the instantaneous energy injection ensuing galaxy outflows $\dot{E}_{\mathrm{kin}}$ (Section 4.2). This fraction ($\sim$10%) is presumably a strong upper limit, considering the large number of ionizing photons emitted by AGNs and star-forming galaxies in the core, and the low density of the ICM. If shocks were dominating the Lyα emission, we could not estimate the mass from Equation (1), but rely on alternative working hypotheses, i.e., pressure equilibrium and geometrical assumptions. Future spectroscopic follow-up will help to quantify the contribution of shocks to the nebular emission, i.e., from UV lines ratios (Dey et al. 2005; Prescott et al. 2009).

3.5. Time Evolution of the Lyα Nebula

The evolution and the lifetime of the Lyα nebula are globally driven by cooling and heating processes, the dynamics of the gas, and their typical associated timescales. In the following, we envisage the time evolution of the system assuming that it is stable and exploring different physical scenarios.

3.5.1. Dynamics

As mentioned in Section 3.2, a single massive nebula at rest at the bottom of the potential well would rapidly collapse and form stars, since the pressure exerted by the particles of a 10^4 K, Lyα-emitting gas would be insufficient to balance the effect of gravity. This scenario is not consistent with our observations (Section 3.3). On the other hand, the Lyα nebula may be globally at rest at the bottom of the potential well if structured in smaller and denser clouds moving with a typical velocity comparable to the velocity dispersion of the cluster. However, the Lyα clouds would dissipate energy through turbulence. If not energized by external factors, they would inevitably start cooling and collapsing. All things considered, if the Lyα nebula were globally at rest in the dark matter halo, it would quickly disappear on a cooling timescale, making our discovery an unconvincingly lucky coincidence. Planned spectroscopic follow-ups will directly probe the dynamical state of the nebula and test our predictions.

3.5.2. Cooling and Heating

Absent a strong powering mechanism, the continuous irradiation of Lyα photons would lead to the quick collapse and disappearance of the clouds. This would happen on timescales of $t_{\mathrm{cool}} \approx 2.07 \times 10^{11}\,\mathrm{s}(T/10^4\,\mathrm{K})\ (n_{\mathrm{e}}/1\,\mathrm{cm}^{-3})^{-1} \times (\Lambda(T)/10^{-23}\,\mathrm{erg\,cm^3\,s^{-1}})^{-1} \sim 0.1\,\mathrm{Myr}$, where $T = 10^4$ K is the gas temperature, $n_{\mathrm{e}} \sim$ 1–10 cm^{-3} the electron density corresponding to plausible values of the volume filling factor ($f = 10^{-3}$–10^{-5}), and $\Lambda(T)$ the cooling function (Sutherland & Dopita 1993; Dey et al. 2005). Strong cooling of the Lyα clouds is disfavored by the large extension of the nebula and the absence of features of recent star formation occurring in the ICM (Section 3.3). Moreover, the cold gas is immersed in a bath of energetic photons produced by the AGN that can keep a large fraction of it ionized. This would be compatible with the geometry of the system and dust absorption (Section 3.3.1). In addition, magnetic fields in the ICM can insulate and stabilize the ionized clouds, further preventing cooling and prolonging their lifetime up to $\sim$10 Myr, as proposed for nebular filaments in local CCs (Conselice et al. 2001; Fabian et al. 2003, 2008). Conversely, Lyα-emitting gas clouds in macroscopic motion with respect to the hot medium, can be thermalized through hydrodynamical instabilities and shocks. We estimate the timescale for the interaction between the cold and hot ICM phases following Klein et al. (1994):

$$t_{\mathrm{therm}} = \left(\frac{n_{\mathrm{e}}^{\mathrm{Ly}\alpha}}{n_{\mathrm{e}}^{\mathrm{hot}}}\right)^{1/2} \frac{R_{\mathrm{cloud}}}{c_{\mathrm{s}}^{\mathrm{hot}}} \tag{4}$$

where R_{cloud} is the radius of individual Lyα-emitting clouds, and $c_{\mathrm{s}}^{\mathrm{hot}} \approx 500\,\mathrm{km\,s^{-1}}$ is the sound speed in the hot medium. This speed is also comparable to the velocity dispersion in the cluster (Section 2.4). For simplicity, we adopted the classical hydrodynamical, non-radiative case where we considered the effects of hot winds moving at a typical speed of the order of $c_{\mathrm{s}}^{\mathrm{hot}}$, much greater than the sound speed in the cold gas. However, a fully numerical treatment including radiative losses gives similar results (Scannapieco & Brüggen 2015). We allowed for possible clumpiness in the nebula assuming $R_{\mathrm{cloud}} < R_{\mathrm{neb}}$ when the volume filling factor is $f < 1$, where $R_{\mathrm{neb}} = 46$ kpc is the radius of the whole nebula (Section 3.1). To constrain R_{cloud}, we adopted a pure geometrical approach (Hennawi & Prochaska 2013). Assuming spherical clumps spatially uniformly distributed in the spherical nebula of radius R_{neb} and with a single uniform clumps' gas density, we can link f to R_{cloud} through the covering factor f_{C}:

$$f = f_{\mathrm{C}} \frac{R_{\mathrm{cloud}}}{R_{\mathrm{neb}}}. \tag{5}$$

The relative smooth morphology of the nebula and the flat surface brightness profile are consistent with f_{C} of the order of unity, though we cannot determine its accurate value. Assuming $f = 10^{-3}$–10^{-5}, we obtain a typical timescale for thermalization of $t_{\mathrm{therm}} \sim$ 0.1–3 Myr. Relaxing the constraint on the covering factor up to a factor of five, we find $t_{\mathrm{therm}} \sim$ 0. 5–10 Myr, consistent with the lower limit on the lifetime of filaments in local CCs.

As a direct consequence, barring an improbable observational coincidence, maintaining the nebula stable against evaporation requires a replenishment of cold gas at a rate of $\dot{M}_{\mathrm{repl}} = M_{\mathrm{Ly}\alpha}/t_{\mathrm{therm}} \gtrsim 1000\ M_{\odot}\,\mathrm{yr}^{-1}$. Note that this estimate is sensitive to the presence of colder gas reservoirs not shining in Lyα and possible localized cooling partially compensating the heating, which could lower the final value. On the other hand, the quoted number could be regarded as a lower limit, since the parameters in the equations could substantially increase the replenishment rate in the plausible ranges we considered. The replenishment rate is directly proportional to f_{C}, but mildly depends on f through both terms of the fraction ($\dot{M}_{\mathrm{repl}} \propto f^{-0.25}$), making the minimum replenishment stable against the range of values we allowed for the filling factor. Physically, the smaller the volume filling factor, the smaller the total mass of the nebula, but the shorter the evaporation time of the denser and

clumpier gas. The density contrast term and the size of the clumps act in opposite ways on $t_{\rm therm}$, with $R_{\rm cloud}$ dominating the final value: smaller clumps are crossed by shocks or hydrodynamical perturbations more rapidly than larger clouds and, consequently, they are disrupted faster.

If not continuously sustained against evaporation, the nebula would disappear on timescales of $t_{\rm therm}$ or, analogously, very short timescales imply unphysical replenishment rates $\dot{M}_{\rm repl}$ to explain the presence of the nebula. We note that the evaporation timescale is shorter than the nebula crossing time (∼90 Myr), given a radius of $R = 46$ kpc and a typical wind speed of 500 km s^{-1} (i.e., Förster Schreiber et al. 2014). This raises the problem of explaining the extension of the nebula, since the Lyα-emitting clouds should evaporate well before filling the observed volume. The issue would be naturally fixed if the clouds primarily form in situ by cooling from the X-ray emitting ICM. Globally, this is unlikely to be the case especially far away from the cluster center, where cooling times from bremsstrahlung are long. However, *local* thermal instabilities might be established in the densest portions of the ICM, providing part of the cold gas needed. On the other hand, if the gas replenishment is due to galaxies (as we envisage in the next section), the size of the nebula is explained both by the distribution of cluster members over a large area, since in this case clouds being injected at different positions would not need to cross the whole nebula, and by recent models of radiatively cooling winds (Thompson et al. 2015). Moreover, galaxies are rapidly moving in the cluster core and, consequently, winds are naturally spread over large portions of the nebula.

4. DISCUSSION

In the previous section, we have shown that the nebula must be constantly replenished of cold gas at a rate of $\gtrsim$1000 $M_\odot$ yr^{-1} in order to shine for timescales longer than ≈10 Myr. Here we focus on galaxy outflows as a plausible mechanism to supply this gas. We introduce independent constraints on the amount of gas released by galaxies based on the observed star formation and AGN activities and we show that outflows are sufficient to explain the presence of the nebula. We further discuss the implications of mass and energy extraction from galaxies and the ensuing injection into the ICM, a process necessary to explain the thermodynamics of local clusters. We also draw a comparison with state-of-the-art cosmological simulations to test the consistency of our estimate.

4.1. Gas Replenishment through Galaxy Outflows

The gas necessary to sustain the Lyα nebula can be supplied by galaxy members through SNe and AGN-driven outflows, a feature ubiquitously observed in high-redshift galaxies (i.e., Newman et al. 2012; Förster Schreiber et al. 2014; Genzel et al. 2014; Harrison et al. 2015) and strongly supported by theoretical models and cosmological and zoom-in simulations (i.e., Davé et al. 2008; Hopkins et al. 2012; Lilly et al. 2013; Gabor & Bournaud 2014). Is the galaxy activity in CL J1449 +0856's core sufficient to provide a minimal mass rate of $\gtrsim$1000 $M_\odot$ yr^{-1} as required by the Lyα nebula? To answer this question, we computed the total mass outflow rate considering both contributions from the observed SFR and AGN activity (Figure 8). We converted members' SFRs into mass outflow rates $\dot{M}_{\rm out}$ by multiplying by a conservative mass loading factor $\eta = \dot{M}_{\rm out}/{\rm SFR} = 1$. This is likely to be a lower limit for the ionized and molecular gas expelled by galaxies, both observationally and theoretically (i.e., Hopkins et al. 2012; Newman et al. 2012; Gabor & Bournaud 2014, Hayword et al. 2015). This order of magnitude is also necessary to explain the metal enrichment of the ICM. Indeed, the same amount of metals is locked into stars and distributed in the ICM, favoring the equality $\dot{M}_{\rm out} \approx$ SFR (i.e., Renzini & Andreon 2014). The SFRs were derived either from SED modeling from our 13-band photometry (S13), Hα from our recent *Subaru*/MOIRCS follow-up (Valentino et al. 2015), or 870 μm continuum detection in ALMA maps applying a main-sequence galaxy template (Magdis et al. 2012). ALMA observations, reduction and analysis will be presented in a forthcoming paper (V. Strazzullo et al. 2016, in preparation). The total SFR in the central region is SFR ≈ 1000 $M_\odot$ yr^{-1}. An individual bright ALMA source stands out in the cluster field. Its 870 μm flux is $F_{870\mu{\rm m}} = 5.5$ mJy, corresponding to a total infrared luminosity between 8–1000 μm of $L_{\rm IR} = 6.\ 6 \times 10^{12}$ L$_\odot$ and SFR = 1100 $M_\odot$ yr^{-1} at $z = 1.99$ (Figure 8). The measurement errors are negligible with respect to the 0.15 dex uncertainty due to modeling (V. Strazzullo et al. 2016, in preparation). As there is no spectroscopic confirmation that the ALMA source is a member of the cluster, we have conservatively excluded it from the SFR accounting. We note that, if confirmed to be part of the cluster, this source would increase by a factor of two times the total SFR in the core.

The growth of black holes further contributes to the mass outflow rates. We estimated its order of magnitude by directly converting $L_{\rm bol}$ into mass outflow rates using the empirical calibration by Cicone et al. (2014). In this case, we obtain ≈600 and 800 $M_\odot$ yr^{-1} for #607 and #661, respectively. Moreover, it appears that we have not captured the system during a phase of exceptional AGN activity. In fact, the integrated SFR/$L_{\rm X}$ ratio observed in the cluster core is close to the cosmic average value (Mullaney et al. 2012). The predicted X-ray luminosity is $\langle L_{\rm X}\rangle$ = SFR × 4.46 × 10^{41} erg s^{-1} ≈4.5 × 10^{44} erg s^{-1}, while the observed value from the two AGNs is 3.4 × 10^{44} erg s^{-1}. We remark that the calibration by Cicone et al. (2014) is based on a sample of local bright IR galaxies with previously known outflows, which, in principle, may overestimate the outflow rates if the relation captures a phase shorter than the AGN duty cycle. On the other side, contribution from phases other than molecular and the uncertain CO luminosity-to-gas mass conversion can increase the outflow rates derived with this calibration. Indeed, strong nuclear ionized winds are now observed in fractions up to 50%–70% of high-redshift AGNs (Harrison et al. 2015), showing how common these features are. Moreover, the calibration by Cicone et al. (2014) is in line with the expectations from simulations reproducing the relations among black hole and galaxy bulge masses or velocity dispersions. In terms of the ratio between the kinematic energy released by AGNs per unit time and their bolometric luminosity, simulations usually assume a coupling efficiency $\epsilon_{\rm f} \sim$ 0.05–0.15 (i.e., Di Matteo et al. 2005; Le Brun et al. 2014 and Section 4.3 below). As we show in Section 4.2.1, the instantaneous kinetic energy associated with AGN and mass outflow rates estimated from the Cicone et al. (2014) relation is indeed ∼5% of the observed bolometric luminosities. Therefore, all things considered, we do include an AGN contribution following Cicone et al. (2014) in our fiducial estimate of the total mass outflow rate. Finally, we note that the reasonable agreement between the replenishment rate estimates from the galaxy activity in the core and from the Lyα nebula

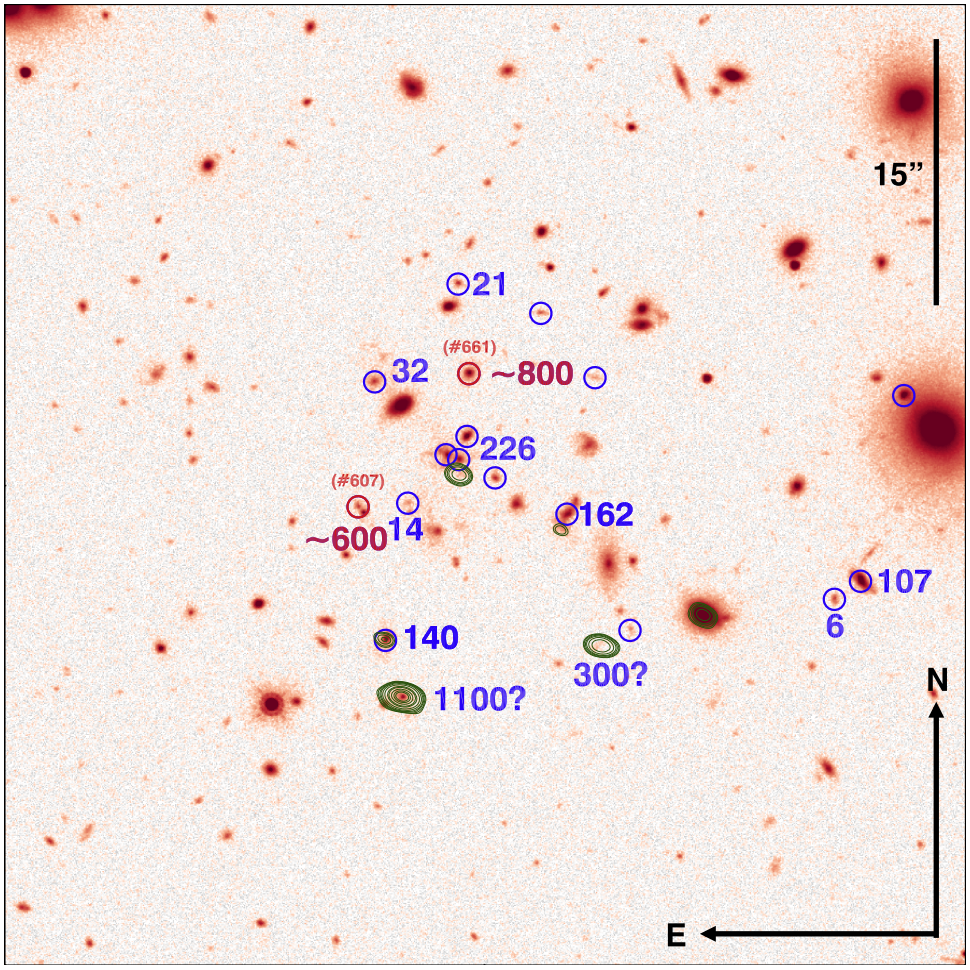

Figure 8. Map of the activity in the central cluster region. For each cluster star-forming (blue circles) or AGN (red circles) member in the *HST*/WFC3 F140W image, we indicate the indirect estimates of the outflow rate in $M_{\odot}$ yr^{-1} as derived in Section 4.1. When available, we provide the SFR estimated from the continuum at 870 μm from ALMA observations (green contours). Question marks denote outflow rates associated with ALMA sources without redshift confirmation and hence not included in our most conservative approach.

would be just incidental if the Lyα emission were predominantly powered by shocks induced by galaxy outflows on the surrounding pressurized ICM (see Section 3.4), suggesting a lesser contribution from this mechanism. In this case, the estimate of the replenishment rate reported in Section 3.5 would not be valid. However, the independent constraint on the energy injection by galactic winds presented in the following section would be unaffected.

4.2. Energy Injection into the ICM

Together with mass, outflows extract energy from galaxies and then deposit it into the surrounding ICM through dissipation, shocks, or turbulence. In the following sections, we estimate the *kinetic* energy injection, neglecting alternative contributions, i.e., from radiation.

4.2.1. Instantaneous Injection

First, we can estimate the *instantaneous* injection of energy at the time of observation:

$$\dot{E}_{\rm kin} = \frac{1}{2}\dot{M}_{\rm out} v^2 \quad (6)$$

where $\dot{M}_{\rm out}$ is the total amount of gas ejected per unit time at $z = 1.99$ by galaxies and v is the outflow velocity. We do not measure v in individual members in our sample, but its statistical average is quite well constrained by increasing samples of high-redshift observations. Therefore, our estimate of $\dot{E}_{\rm kin}$ should be taken in a statistical sense. We assign a wind speed of 500 km s^{-1} to SN-driven outflows for each star-forming galaxy, while for AGN-driven outflows, we assume a typical speed of 1000 km s^{-1} (Cicone et al. 2014; Förster Schreiber et al. 2014; Genzel et al. 2014). Given the baseline mass outflow rate in Section 4.1, we obtain $\dot{E}_{\rm kin}(z = 1.99) \sim 5 \times 10^{44}$ erg s^{-1}. This energy is a factor of 20 times (5 times) larger than the observed Lyα (X-ray) extended luminosity. The five times factor with respect to the X-ray luminosity is sufficient to offset the global radiative cooling of the hot plasma. Assuming the balance between heating and the observed cooling rate as in local clusters would thus imply an energy injection five times lower than estimated above. However, net heating is necessary to justify the presence of the Lyα nebula, since the cooling from the X-ray globally occurs on long timescales and is not sufficient to explain the Lyα emission (Section 3.3.4). The injected energy is coming predominantly from AGN activity (~85%) with a non-negligible contribution from star formation (~15%), while, in terms of mass, AGNs are responsible for up to two-thirds of the total gas released into the ICM. SFGs would dominate the mass and energy injection only if

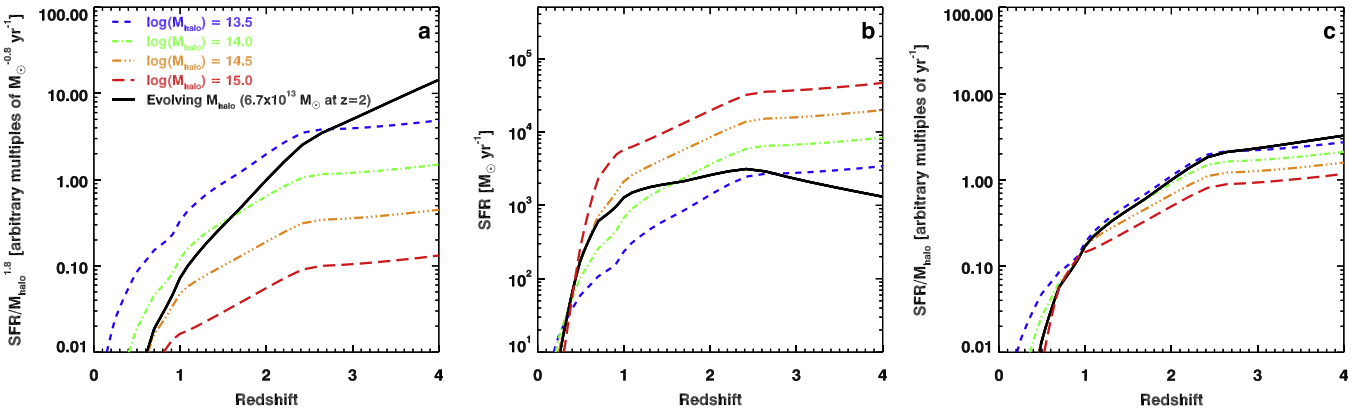

Figure 9. Expected efficacy of outflow energy injection as a function of halo mass and redshift. Based on the empirical mapping of the star formation and galaxy clustering evolution through cosmic time (Béthermin et al. 2013), we model the redshift evolution of the outflow energy injection over the thermal energy of the ICM (panel (a)). The mechanical energy injection scales as the integrated SFR in the halo, while the total thermal energy of the hot ICM increases as $E_{\rm therm} \propto T_{\rm vir}\, M_{\rm gas} \propto M_{\rm halo}^{1.8}$, assuming a gas fraction varying with the halo mass (Renzini & Andreon 2014). Hence, the y axis in panel (a) represents the "efficacy" of the energy injection. In panel (b), we show the evolution of the SFR as a function of redshift and halo mass in Béthermin et al. (2013). The ratio SFR/$M_{\rm halo}$ changes slowly between $2 < z < 4$ (panel (c)).

we largely overestimated the contribution from AGNs. We note that CL 1449+0856 is not anomalous in terms of star formation activity with respect to potentially similar structures at comparable redshift (i.e., Tran et al. 2010; Yuan et al. 2014; Gobat et al. 2015; Santos et al. 2015) and it is globally consistent with the tracks reported in Figure 9 based on the model by Béthermin et al. (2013). The instantaneous energy input from AGN corresponds only to 0.05 $L_{\rm bol}^{\rm AGN}$, a factor of three times lower than typically assumed in simulations (Section 4.3), supporting the estimate of the mass outflow rates reported in Section 4.1, while from star formation it is just 0.003 $L_{\rm bol}^{\rm SFGs}$. In general, given the SFR/$L_{\rm X}$ cosmic average (Mullaney et al. 2012) and the adopted calibrations, we expect AGN outflows to provide 5–10 times more energy than winds induced by star formation.

4.2.2. Integrated Energy Injection

We can now estimate the *total* energy injection up to $z = 1.99$, integrating $\dot{E}_{\rm kin}$ over time prior to observation:

$$E_{\rm kin} = \int_{t(z \geqslant 1.99)} \dot{E}_{\rm kin}\, dt. \quad (7)$$

For simplicity, we assume that the *instantaneous* energy injection is proportional to the SFR:

$$\dot{E}_{\rm kin} = \beta\ {\rm SFR} \quad (8)$$

where $\beta(z = 1.99) \sim 1.6 \times 10^{49}$ erg $M_{\odot}^{-1}$. Then from Equation (7),

$$\begin{aligned} E_{\rm kin} &= \int_{t(z \geqslant 1.99)} \beta\ {\rm SFR}(t)\, dt \\ &= \frac{\beta}{1 - R} \int_{t(z \geqslant 1.99)} {\rm SFR}(t)(1 - R)\, dt \\ &= \frac{\beta}{1 - R}\, M_{\star} \end{aligned} \quad (9)$$

where $M_{\star}$ is the total stellar mass of $2 \times 10^{12}\ M_{\odot}$ observed at $z = 1.99$ (Section 2.4 and S13) and $R = 0.4$ is the mass return into the interstellar medium (Bruzual & Charlot 2006). Eventually, we obtain $E_{\rm kin} = 5 \times 10^{61}$ erg. Considering a universal baryon fraction of $f_{\rm b} = 0.15$ in the ICM (Planck Collaboration XVI et al. 2014), the total energy per particle in the hot ICM then is ∼2 keV. This value is ∼10% of the binding energy of the halo at $z = 1.99$ and of the same order of magnitude in cluster progenitors. Hence, part of the ICM particles might have been expelled by the structure at some early stage. The integrated energy is also comparable to the thermal energy per particle $E_{\rm therm} = 3/2\ kT$. Indeed, assuming virialization, $kT = kT_{\rm vir} = GM_{\rm halo}\mu {\rm m_p}/2R_{\rm vir} \sim 1.9$ keV and, thus, $E_{\rm therm} \sim 2.8$ keV. This is an order of magnitude estimate, as the structure is unlikely to be fully virialized at this stage—simulations suggest a thermodynamic temperature that is 15%–20% smaller than $T_{\rm vir}$ (Section 4.3). We stress here that our estimate of the integrated energy injection is affected by uncertainties on the total mass outflow rate, outflow velocities, the halo mass, and its baryon content and it depends on the assumptions we described. All things considered, the estimate may well increase or decrease by a factor of ∼0.5 dex.

This approach relies on the use of $M_{\star}$ in CL J1449+0856 as a proxy for the total mass ejected through outflows in the past. This presumes the adoption of a mass loading factor of $\eta = 1$ and that v depends on local galaxy properties not evolving with time. The advantage of using $M_{\star}$ is the straightforward inclusion of the contribution to the energy injection by galaxies active in the past, but observed to be passive at $z = 1.99$. However, there are two important assumptions behind this results: first, we suppose that the total AGN mass outflow rate is proportional to the total SFR at any time and second, that β is constant with time.

4.2.3. Caveats

We justify the first assumption considering that SFR and AGN activity are correlated (Mullaney et al. 2012): statistically, on large samples the average AGN X-ray luminosity is equal to $\langle L_{\rm X} \rangle = {\rm SFR} \times 4.46 \times 10^{41}$ erg s^{-1}. Nevertheless, the AGN mass outflow rate might depend nonlinearly on the AGN luminosity. For example, in the empirical relation by Cicone et al. (2014), $\dot{M}_{\rm out} \propto L_{\rm bol}^{\rm b}$ with b = 0.72. From Equation (6),

this nonlinear term becomes

$$\dot{E}_{\rm kin}^{\rm AGN} = \frac{1}{2}\dot{M}_{\rm out}^{\rm AGN} v_{\rm AGN}^2 = k_1 L_{\rm X}^{0.72} = k_2\ {\rm SFR}^{0.72} \quad (10)$$

where k_1 and k_2 are constants including the bolometric correction linking $L_{\rm X}$ and $L_{\rm bol}$, the velocity term $v^2/2$, and the coefficients in the Cicone et al. (2014) and Mullaney et al. (2012) relations. Simply combining Equations (8) and (10), we obtain

$$\beta = c_1 + c_2\ {\rm SFR}^{0.72-1} \quad (11)$$

where c_1 and c_2 are constants. Thus, the nonlinear term introduced by the AGN mass outflow rate impacts our result only when the total SFR in the progenitors of CL J1449+0856 drops significantly. Equation (11) justifies also our second main assumption that β is roughly constant with time, depending only on numeric constants and the total SFR in all the cluster progenitors.

Does the total SFR in the cluster progenitors evolve with redshift? At $z > 1.99$, the SFR is spread over several subhalos that will form the observed cluster by merging. Here we trace the growth of individual dark matter halos from simulations using the Fakhouri et al. (2010) model. According to Béthermin et al. (2013), in each subhalo, the total SFR peaks at $z \sim 2$ and then slowly decreases (black curve in Figure 9, panel (b)). However, to compute the total SFR contributing to the energy injection over time, we have to consider *all* of the subhalos. This corresponds to normalizing the individual SFR to the halo mass at each redshift (Figure 9, panel (c)). In this case, the function $X(z) = \langle {\rm SFR}(z)\rangle / M_{\rm halo}(z)$ mildly increases with redshift. Thus, the nonlinear term in Equation (11) becomes less important with redshift.

4.2.4. Final Remarks

We attempted an alternative estimate of the total kinetic energy purely base on the tracks in Figure 9. We obtain $E_{\rm kin} \sim 5 \times 10^{61}$ erg released by galaxies over $2 < z < 4$ computed as

$$E_{\rm kin} = \frac{1}{2}\,\dot{M}_{\rm repl} v^2 \int_{t(z=4)}^{t(z=2)} \frac{X(t(z))}{X(t(z=2))}\,dt \quad (12)$$

where the function $X(z) = \langle {\rm SFR}(z)\rangle / M_{\rm halo}(z)$ accounts for the expected flat trend of $\langle {\rm SFR}\rangle$ at $2 < z < 4$ and incorporates the integrated activity spread in halo progenitors of lower masses (Figure 9, panel (c)). The net effect of the integral is an increase of the time interval, from 1.7 Gyr between $2 < z < 4$ to 4.4 Gyr. This result is consistent with the one presented above, providing ~2 keV per particle in the hot ICM, assuming a universal baryon fraction $f_{\rm b} = \Omega_{\rm b}/\Omega_{\rm m} = 0.15$.

Here we limit the integral to $z = 4$, before which the masses of individual progenitor halos rapidly become similar to individual galaxy halos ($\approx 1 \times 10^{13}\ M_\odot$ following Fakhouri et al. 2010). At these masses, fast winds would have easily expelled the material from the halo, that later would have been reaccreted with the halo growth. However, observed properties of local structures may disfavor this scenario for energy injection (Ponman et al. 2003).

We note that the tracks in Figure 9 are calibrated on the observed stellar mass function of passive and star-forming galaxies residing in halos of masses of $11.5 < M_{\rm halo} < 13.5$ at high redshift. However, the model does not assume any environmental dependence of galaxy properties, prominent at lower redshift. The transformation of *cluster* galaxies into red, passive, early-type systems at low redshift makes the predicted SFR a likely overestimation at $z \lesssim 1.5$ (Popesso et al. 2015). Below $z \sim 1.5$ the outflow energy contribution to the ICM is expected to be negligible with respect to the internal energy, as shown in Figure 9. We remark here that we do not make any prediction on the later growth of a massive central galaxy and its associated black hole, whose "radio" maintenance feedback looks necessary to avoid overcooling in the cluster core (McNamara & Nulsen 2007; Fabian 2012; Gaspari et al. 2012).

4.3. Comparison with Cosmological Simulations

We compared our observational results with the total energy injected by black holes into the ICM of systems similar to CL J1449+0856 at $z = 2$ in simulations. We used the two models from the suite of hydrodynamical cosmological simulations presented in Le Brun et al. (2014), which form an extension to the Overwhelmingly Large Simulations project (OWLS, Schaye et al. 2010). The first is a standard non-radiative model (NOCOOL), while the second further includes prescriptions for metal-dependent radiative cooling, star formation, stellar evolution, mass loss, chemical enrichment, stellar feedback, and AGN feedback. Among the models described in Le Brun et al. (2014), we selected the AGN 8.0 model as it provides the best match to the X-ray, Sunyaev-Zel'dovich, and optical observations of local groups and clusters (Le Brun et al. 2014; McCarthy et al. 2014). In these two models, we selected the halos with $M_{200} = (5\text{–}7) \times 10^{13}\ M_\odot$ at $z = 2$ (yielding respectively 79 and 91 such systems in the AGN 8.0 and NOCOOL physical models). For each of these structures, we computed the mass-weighted temperature within a 300 kpc aperture, the mean entropy $S = kT/n_{\rm e}^{2/3}$ within $0.15\,R_{500}$, the virial temperature $kT_{\rm vir}$, and the binding energy. The energy injected by all the black holes lying within R_{500} is $E_{\rm inj} = M_{\rm BH}(<R_{500})c^2\epsilon_{\rm f}\,\epsilon_{\rm r}/(1-\epsilon_{\rm r})$, where $\epsilon_{\rm r} = 0.1$ is the radiative efficiency of the black hole accretion disk, $\epsilon_{\rm f} = 0.15$ the efficiency of the coupling of the AGN feedback to the gas, and c the speed of light. We estimate the average injected energy per particle assuming $f_{\rm b} M_{500}/\mu {\rm m_p}$ baryonic particles in the ICM, where $f_{\rm b} = 0.15$ is the universal baryon fraction (Planck Collaboration XVI et al. 2014), $\mu = 0.6$ is the mean molecular weight, and $m_{\rm p}$ is the proton mass. We obtain that the mean injected energy is of the order of 8×10^{61}erg ($\approx$2.8 keV per particle, Figure 10, panel (a)), which is of the same order of magnitude as the typical binding energy of the selected systems. Using M_{200} instead of M_{500} in the definition of the number of particles reduces the estimate by a factor of 1.4 times. However, we stress that this is a rough estimate of the overall effect on the whole ICM, while in the simulations the energy injection is effective mostly in a small region surrounding the AGN. All things considered, this estimate is fully consistent with our observational estimate of ~2 keV per particle. The mean temperature increases from 1.44 keV to 1.73 keV when efficient AGN feedback is included (Figure 10, panel (b)). Moreover, the entropy within $0.15\,R_{500}$, tracing non-gravitational heating and cooling, increases from 19.9 keV cm^2 to 58.0 keV cm^2 (Figure 10, panel (c)). As the mean baryonic fraction within R_{500} decreases from 14% in the non-radiative model to 10.7% in the AGN 8.0 model, some of the gas, which should have been contained within R_{500} in the absence of AGN feedback, has been ejected, similarly to what was previously found for progenitors of $z = 0$ groups (McCarthy et al. 2011, but see Pike et al. 2014 who find that most of the AGN feedback energy is released at $z < 1$ in their simulated

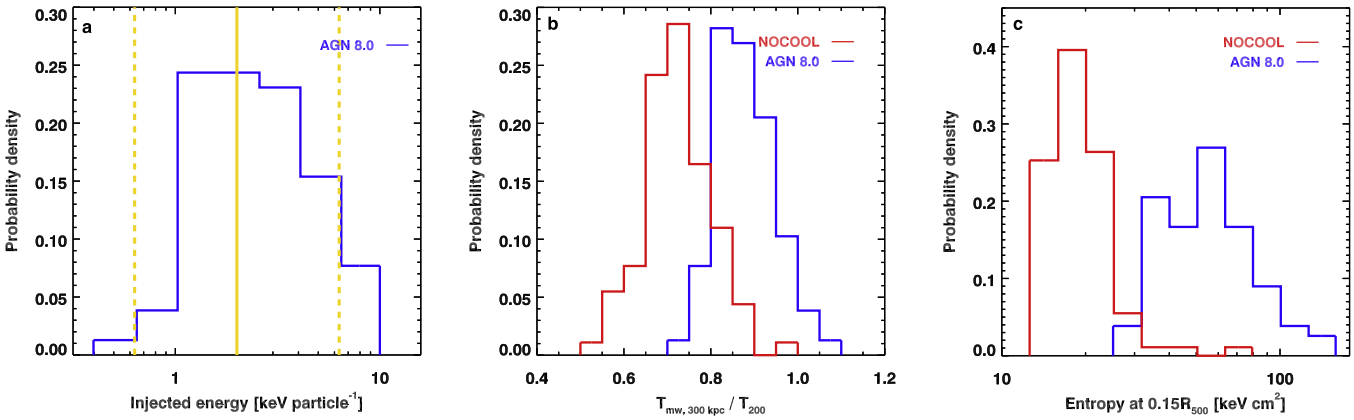

Figure 10. Temperature and entropy increase in $z = 2$ clusters when AGN feedback is active in simulations. We show the distribution of the energy per particle injected in $M_{200} = (5–7) \times 10^{13}\ M_{\odot}$ systems at $z = 2$ when AGN feedback is turned on in our suite of cosmo-OWLS simulations (panel (a)) and its effect on the mass-weighted temperature within 300 kpc in units of the virial temperature $kT_{\rm vir}$ (panel (b)) and entropy at $0.15R_{\rm vir}$ (panel (c)). Blue lines indicate the reference AGN 8.0 feedback model, while red lines mark the non-radiative model (Le Brun et al. 2014). The yellow lines in panel (a) show our fiducial estimate of ~2 keV per particle from observations and a 0.5 dex uncertainty.

clusters). Overall, this set of cosmological simulations predicts an energy injection due to AGN of the same order of magnitude of our estimate based on the average properties of galaxy outflows.

4.4. Future Lyα Surveys of High-redshift Clusters

The energy injection scenario based on galaxy outflows replenishing huge gas reservoirs of cold and warm gas should apply for structures similar to CL J1449+0856 and comply with the general increase of star formation and AGN activity observed in high-redshift galaxies. Do we thus expect to see giant Lyα nebulae in all massive cluster progenitors? The answer could be negative. In fact, AGN activity—which illuminates the gas expelled through outflows and keeps it ionized—might be a prerequisite for the presence of Lyα systems. Absent a powerful ionizing source, dense environments hosting strong star formation activity might not show any extended Lyα blob. This might be the case for the massive halo inside the proto-cluster region at $z = 3.09$ in the SSA22 field (Steidel et al. 2000; Kubo et al. 2015). A statistical assessment of the number of active galaxies in clusters at each stage of their evolution is important to address this issue. Nevertheless, galaxy outflows remain a ubiquitous feature of high-redshift galaxies. Are the massive gas reservoirs replenished by outflows destined to collapse and form stars according to their cooling and free-fall time? The gas in outflows is not at rest by definition. Moreover both simulations (Bournaud et al. 2014) and observations (Martin & Bouché 2009) show that outflows accelerate at larger radii because of pressure gradients in steady-state flows. This results in long collapse timescales, possibly preventing the formation of stars spread over several tens of kiloparsecs. The assembly of larger samples of clusters progenitors will allow us to test these predictions.

5. CONCLUSIONS

In this work, we presented the discovery of a giant 100 kpc extended Lyα nebula in the core of a $5–7 \times 10^{13}\ M_{\odot}$, X-ray detected cluster at $z = 1.99$. This discovery reveals the coexistence of warm ionized blobs and the hot intergalactic medium and extends the known relation between Lyα nebulae and overdense regions of the universe to the dense core of a relatively mature cluster. We pinpointed two X-ray AGNs as the most likely candidates to power the nebula, disfavoring ionization from very young stars and cooling from the X-ray phase in the form of a stationary classical cooling flow. In principle, regulated cooling as in local cool-core clusters could partially contribute to the Lyα luminosity, but several inconsistencies between CL J1449+0856 and local systems are evident. Above all, the ratio between the Lyα luminosity and the total X-ray luminosity is a factor 10–1000 times higher in CL J1449+0856 than in local CCs even in those cases where strong radio-sources are present (i.e., Perseus). Dissipation of mechanical energy injected by galaxy outflows may also contribute to the total Lyα luminosity. The interaction between the Lyα nebula and the surrounding hot ICM requires a $\gtrsim$1000 $M_{\odot}\ {\rm yr}^{-1}$ gas replenishment rate to sustain the nebula against evaporation. We explore galaxy outflows in the cluster core as a possible source of gas supply and find that the generous total SFR ($\approx$1000 $M_{\odot}\ {\rm yr}^{-1}$) and the outflow rate owing to the growth of supermassive black holes ($\approx$1400 $M_{\odot}\ {\rm yr}^{-1}$) are sufficient to replenish the nebula. This directly implies a significant injection of kinetic energy into the ICM up to $\approx$2 keV per particle, in agreement with the predictions from the cosmo-OWLS simulations and with constraints set by the thermodynamic properties of local massive structures. In our baseline scenario, the AGN channel provides up to 85% of the total injected energy, with the rest supplied by star formation through SNe-driven winds. The instantaneous energy injection exceeds by a factor of five times the current X-ray luminosity, offsetting the global cooling from the X-ray phase. Nevertheless, the high star formation and black hole accretion rates deep in the potential well of this cluster support the general increase in galaxy activity observed in similar structures at comparable redshift and challenge the current prescriptions on the fueling by cosmological cold flows penetrating in massive halos. If this structure is not just a curious anomaly, the potential presence of cold streams despite its high mass would lead to important consequences on the "halo quenching" mechanism and, thus, on galaxy formation and evolution in general.

The advent of forthcoming facilities will allow us to drastically reduce observational uncertainties and avoid a heavy resort to assumptions. Measurements of temperature, pressure, and entropy profiles of the hot ICM in young clusters will be possible with the foreseen Athena X-ray satellite, while the systematic follow-up of Lyα emission in clusters at $z > 2–3$ could start soon with new wide-field integral field spectrographs on large telescopes, like

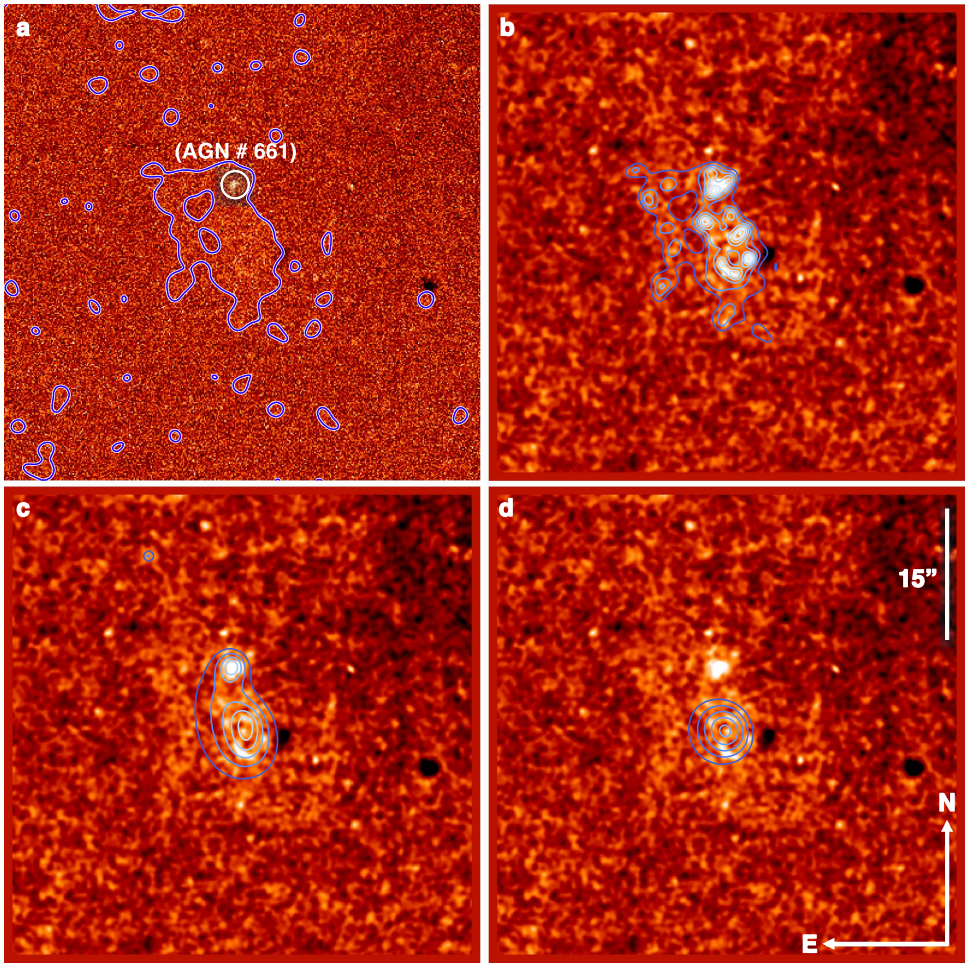

Figure 11. Wavelet reconstruction of the Lyα image. We show the original unsmoothed Lyα emission line map of the central region of CL J1449+0856 in panel (a). The 1σ contour of the large-scale Lyα emission from the wavelet reconstruction (blue line) and the X-ray obscured AGN (white circle) are marked for reference. Panels (b)–(d) show the reconstructed wavelet contours at $\geqslant 1\sigma$, $\geqslant 3\sigma$, and $\geqslant 5\sigma$, respectively, (blue lines) of the Lyα emission line map. Point-like sources have been subtracted before computing the surface brightness contours. The number of contours is arbitrary and chosen to pinpoint the peak of the extended emission. For reference, 15″ corresponds to ∼125 kpc at $z = 1.99$.

MUSE and KCWI. Spectroscopy in the ultra-violet range provides crucial information on the kinematics of the nebula, the metal enrichment, and its main powering mechanism. If the scenario we propose here is correct, we expect the Lyα nebula to show signatures of complex motion due to outflows and to be fairly metal-rich. Eventually, the arising coherent scenario we sketch could help us to understand the global early evolution of massive structures.

We acknowledge the constructive comments of the referee and we thank Daniel Perley for support during the reduction of Keck/LRIS data with his pipeline. Some of the data presented therein were obtained at the W.M. Keck Observatory, which is operated as a scientific partnership among the California Institute of Technology, the University of California and the National Aeronautics and Space Administration. Keck telescope time was granted by NOAO (Prop. ID: 2014A-0131), through the Telescope System Instrumentation Program (TSIP). TSIP is funded by NSF. The Observatory was made possible by the generous financial support of the W.M. Keck Foundation. The authors wish to recognize and acknowledge the very significant cultural role and reverence that the summit of Mauna Kea has always had within the indigenous Hawaiian community. We are most fortunate to have the opportunity to conduct observations from this mountain. The scientific results reported in this article are also based in part on observations made by the *Chandra* X-ray Observatory. A.F. acknowledges the *Chandra* grant GO4-15133A to UMBC. This paper also makes use of the following ALMA data: ADS/JAO. ALMA#2012.1.00885.S. ALMA is a partnership of ESO (representing its member states), NSF (USA) and NINS (Japan), together with NRC (Canada), NSC and ASIAA (Taiwan), and KASI (Republic of Korea), in cooperation with the Republic of Chile. The Joint ALMA Observatory is operated by ESO, AUI/NRAO, and NAOJ. We acknowledge financial support from the Agence Nationale de la Recherche (contracts #ANR-12-JS05-0008-01) and the EC through the European Research Council Starting grants StG-257720 and StG-240039, and the Advanced grant FP7-340519.

APPENDIX

We show the unsmoothed Lyα image from the Keck/LRIS narrow-band follow-up of CL J1449+0856 in panel (a) of Figure 11. The only purpose is to demonstrate that the Lyα emission is not dominated by individual galaxies, but it is

distributed fairly homogeneously over several square arcseconds. The very low surface brightness regimes probed in this image make the identification of the nebula difficult by eye. It is easier to recognize it comparing the original narrow- and broadband images shown in Figure 2 or, alternatively, with a moderate smoothing (1″, Figures 2 and 11 panels (b)–(d)). To guide the eye and pinpoint the peak of the extended emission, in panels (b)–(d) of Figure 11, we show the contours of the wavelet reconstructed Lyα image. In each panel, we show the contours after the subtraction of point-like sources, retaining only the signal on larger scales, namely the Lyα nebula. Panel (b) shows the maximum extension of the Lyα nebula, while the smoother denoised contours in panels (c) and (d) allow for the identification of the peak of the extended emission. The appearance of two peaks in panel (c) depends on the number of scales adopted to slice the image with the wavelet technique and does not affect the main findings of this work. The region spanned by the $\geqslant 5\sigma$ detection in panel (d) is the same used to measure the extended continuum emission (Section 2.2). In every panel, the number of contours is chosen arbitrarily to highlight the peak of the emission and do not correspond to a fix step in surface brightness.

REFERENCES

Andreon, S., Maughan, B., Trinchieri, G., & Kurk, J. 2009, A&A, 507, 147
Arnaud, M., Pratt, G. W., Piffaretti, R., et al. 2010, A&A, 517, A92
Arrigoni-Battaia, F., Hennawi, J. F., Prochaska, J. X., & Cantalupo, S. 2015, ApJ, 809, 163
Bayer-Kim, C. M., Crawford, C. S., Allen, S. W., Edge, A. C., & Fabian, A. C. 2002, MNRAS, 337, 938
Béthermin, M., Wang, L., Doré, O., et al. 2013, A&A, 557, A66
Borisova, E., Cantalupo, S., Lilly, S. J., et al. 2016, arxiv:1605.01422
Bournaud, F., Perret, V., Renaud, F., et al. 2014, ApJ, 780, 57
Bower, R. G., Morris, S. L., Bacon, R., et al. 2004, MNRAS, 351, 63
Brodwin, M., McDonald, M., Gonzalez, A. H., et al. 2015, arxiv:1504.01397
Brusa, M., Comastri, A., Daddi, E., et al. 2005, A&A, 432, 69
Bruzual, G., & Charlot, S. 2006, MNRAS, 344, 1000
Bunker, A. J., Warren, S. J., Hewett, P. C., & Clements, D. L. 1995, MNRAS, 273, 513
Campisi, M. A., Vignali, C., Brusa, M., et al. 2009, A&A, 501, 485
Cantalupo, S., Arrigoni-Battaia, F., Prochaska, J. X., Hennawi, J. F., & Madau, P. 2014, Natur, 506, 63
Cantalupo, S., Porciani, C., Lilly, S. J., & Miniati, F. 2005, ApJ, 628, 61
Churazov, E., Brüggen, M., Kaiser, C. R., Böhringer, H., & Forman, W. 2001, ApJ, 554, 261
Cicone, C., Maiolino, R., Sturm, E., et al. 2014, A&A, 562, A21
Conselice, C. J., Gallagher, J. S., III, & Wyse, R. F. G. 2001, AJ, 122, 2281
Cowie, L. L., Fabian, A. C., & Nulsen, P. E. J. 1980, MNRAS, 191, 399
Crawford, C. S., & Fabian, A. C. 1989, MNRAS, 239, 219
Daddi, E., Bournaud, F., Walter, F., et al. 2010, ApJ, 713, 686
Danovich, M., Dekel, A., Hahn, O., Ceverino, D., & Primack, J. 2015, MNRAS, 449, 2087
Davé, R., Oppenheimer, B. D., & Sivanandam, S. 2008, MNRAS, 391, 110
Dekel, A., Birnboim, Y., Engel, G., et al. 2009, Natur, 457, 451
Dey, A., Bian, C., Soifer, B. T., et al. 2005, ApJ, 629, 654
Di Matteo, T., Springel, V., & Hernquist, L. 2005, Natur, 433, 604
Dijkstra, M., Haiman, Z., & Spaans, M. 2006, ApJ, 649, 37
Elvis, M., Wilkes, B. J., McDowell, J. C., et al. 1994, ApJS, 95, 1
Fabian, A. C. 2012, ARA&A, 50, 455
Fabian, A. C., Crawford, C. S., Johnstone, R. M., & Thomas, P. A. 1987, MNRAS, 228, 963
Fabian, A. C., Johnstone, R. M., Sanders, J. S., et al. 2008, Natur, 454, 968
Fabian, A. C., Nulsen, P. E. J., & Arnaud, K. A. 1984a, MNRAS, 208, 179
Fabian, A. C., Nulsen, P. E. J., & Canizares, C. R. 1984b, Natur, 310, 733
Fabian, A. C., Sanders, J. S., Crawford, C. S., et al. 2003, MNRAS, 344, L48
Fakhouri, O., Ma, C.-P., & Boylan-Kolchin, M. 2010, MNRAS, 406, 2267
Finoguenov, A., Guzzo, L., Hasinger, G., et al. 2007, ApJS, 172, 182
Förster Schreiber, N. M., Genzel, R., Newman, S. F., et al. 2014, ApJ, 787, 38
Francis, P. J., Woodgate, B. E., Warren, S. J., et al. 1996, ApJ, 457, 490
Gabor, J. M., & Bournaud, F. 2014, MNRAS, 441, 1615
Gaspari, M., Ruszkowski, M., & Sharma, P. 2012, ApJ, 746, 94
Geach, J. E., Alexander, D. M., Lehmer, B. D., et al. 2009, ApJ, 700, 1
Genzel, R., Förster Schreiber, N. M., Rosario, D., et al. 2014, ApJ, 796, 7
George, M. R., Leauthaud, A., Bundy, K., et al. 2011, ApJ, 742, 125
Gobat, R., Daddi, E., Béthermin, M., et al. 2015, A&A, 581, A56
Gobat, R., Daddi, E., Onodera, M., et al. 2011, A&A, 526, A133
Gobat, R., Strazzullo, V., Daddi, E., et al. 2013, ApJ, 776, 9
Goerdt, T., Dekel, A., Sternberg, A., et al. 2010, MNRAS, 407, 613
Harrison, C. M., Alexander, D. M., Mullaney, J. R., et al. 2015, arxiv:1511.00008
Hatch, N. A., Crawford, C. S., & Fabian, A. C. 2007, MNRAS, 380, 33
Hatch, N. A., Crawford, C. S., Fabian, A. C., & Johnstone, R. M. 2005, MNRAS, 358, 765
Hatch, N. A., Overzier, R. A., Röttgering, H. J. A., Kurk, J. D., & Miley, G. K. 2008, MNRAS, 383, 931
Hayward, C. C., & Hopkins, P. F. 2015, arXiv:1510.05650, MNRAS submitted
Heckman, T. M., Baum, S. A., van Breugel, W. J. M., & McCarthy, P. 1989, ApJ, 338, 48
Heckman, T. M., Kauffmann, G., Brinchmann, J., et al. 2004, ApJ, 613, 109
Hennawi, J. F., & Prochaska, J. X. 2013, ApJ, 766, 58
Hopkins, P. F., Quataert, E., & Murray, N. 2012, MNRAS, 421, 3522
Kaiser, N. 1991, ApJ, 383, 104
Kennicutt, R. C., Jr. 1998, ARA&A, 36, 189
Klein, R. I., McKee, C. F., & Colella, P. 1994, ApJ, 420, 213
Kubo, M., Yamada, T., Ichikawa, T., et al. 2016, MNRAS, 455, 3333
Le Brun, A. M. C., McCarthy, I. G., & Melin, J.-B. 2015, MNRAS, 451, 3868
Le Brun, A. M. C., McCarthy, I. G., Schaye, J., & Ponman, T. J. 2014, MNRAS, 441, 1270
Leauthaud, A., Finoguenov, A., Kneib, J.-P., et al. 2010, ApJ, 709, 97
Ledlow, M. J., Voges, W., Owen, F. N., & Burns, J. O. 2003, AJ, 126, 2740
Lilly, S. J., Carollo, C. M., Pipino, A., Renzini, A., & Peng, Y. 2013, ApJ, 772, 119
Lusso, E., Comastri, A., Simmons, B. D., et al. 2012, MNRAS, 425, 623
Magdis, G. E., Daddi, E., Béthermin, M., et al. 2012, ApJ, 760, 6
Martin, C. L., & Bouché, N. 2009, ApJ, 703, 1394
Matsuda, Y., Yamada, T., Hayashino, T., et al. 2004, AJ, 128, 569
McCarthy, I. G., Le Brun, A. M. C., Schaye, J., & Holder, G. P. 2014, MNRAS, 440, 3645
McCarthy, I. G., Schaye, J., Bower, R. G., et al. 2011, MNRAS, 412, 1965
McCarthy, P. J., Spinrad, H., Dickinson, M., et al. 1990, ApJ, 365, 487
McDonald, M., Veilleux, S., Rupke, D. S. N., & Mushotzky, R. 2010, ApJ, 721, 1262
McNamara, B. R., & Nulsen, P. E. J. 2007, ARA&A, 45, 117
McNamara, B. R., Russell, H. R., Nulsen, P. E. J., et al. 2014, ApJ, 785, 44
Miley, G. K., Overzier, R. A., Zirm, A. W., et al. 2006, ApJL, 650, L29
Mullaney, J. R., Daddi, E., Béthermin, M., et al. 2012, ApJL, 753, L30
Navarro, J. F., Frenk, C. S., & White, S. D. M. 1997, ApJ, 490, 493
Newman, S. F., Genzel, R., Förster-Schreiber, N. M., et al. 2012, ApJ, 761, 43
O'Dea, K. P., Quillen, A. C., O'Dea, C. P., et al. 2010, ApJ, 719, 1619
Osterbrock, D. E., & Ferland, G. J. 2006, Astrophysics of Gaseous Nebulae and Active Galactic Nuclei (Sausalito, CA: Univ. Sci. Books)
Papovich, C., Momcheva, I., Willmer, C. N. A., et al. 2010, ApJ, 716, 1503
Peterson, J. R., & Fabian, A. C. 2006, PhR, 427, 1
Piconcelli, E., Jimenez-Bailón, E., Guainazzi, M., et al. 2005, A&A, 432, 15
Pike, S. R., Kay, S. T., Newton, R. D. A., Thomas, P. A., & Jenkins, A. 2014, MNRAS, 445, 1774
Planck Collaboration XVI, Ade, P. A. R., Aghanim, N., Armitage-Caplan, C., et al. 2014, A&A, 571, A16
Ponman, T. J., Cannon, D. B., & Navarro, J. F. 1999, Natur, 397, 135
Ponman, T. J., Sanderson, A. J. R., & Finoguenov, A. 2003, MNRAS, 343, 331
Popesso, P., Biviano, A., Finoguenov, A., et al. 2015, A&A, 579, A132
Prescott, M. K. M., Dey, A., & Jannuzi, B. T. 2009, ApJ, 702, 554
Prescott, M. K. M., Dey, A., & Jannuzi, B. T. 2012, ApJ, 748, 125
Prescott, M. K. M., Dey, A., & Jannuzi, B. T. 2013, ApJ, 762, 38
Renzini, A., & Andreon, S. 2014, MNRAS, 444, 3581
Salomé, P., Combes, F., Revaz, Y., et al. 2011, A&A, 531, A85
Salpeter, E. E. 1955, ApJ, 121, 161
Santos, J. S., Altieri, B., Valtchanov, I., et al. 2015, MNRAS, 447, L65
Santos, J. S., Fassbender, R., Nastasi, A., et al. 2011, A&A, 531, L15
Scannapieco, E., & Brüggen, M. 2015, ApJ, 805, 158
Schaerer, D. 2003, A&A, 397, 527
Schaye, J., Dalla Vecchia, C., Booth, C. M., et al. 2010, MNRAS, 402, 1536
Sharma, P., McCourt, M., Quataert, E., & Parrish, I. J. 2012, MNRAS, 420, 3174

Spitzer, L. 1978, Physical Processes in the Interstellar Medium (New York, NY: Wiley)
Stanford, S. A., Brodwin, M., Gonzalez, A. H., et al. 2012, ApJ, 753, 164
Starck, J. L., Saber Naceur, M., & Murtagh, R. 2010, in 6th Astronomical Data Analysis Conf. http://www.aset.org.tn/conf/ADA6/online_presentations.php
Steidel, C. C., Adelberger, K. L., Shapley, A. E., et al. 2000, ApJ, 532, 170
Strazzullo, V., Gobat, R., Daddi, E., et al. 2013, ApJ, 772, 118
Sutherland, R. S., & Dopita, M. A. 1993, ApJS, 88, 253
Tacconi, L. J., Neri, R., Genzel, R., et al. 2013, ApJ, 768, 74
Thompson, T. A., Fabian, A. C., Quataert, E., & Murray, N. 2015, MNRAS, 449, 147
Tozzi, P., & Norman, C. 2001, ApJ, 546, 63
Tran, K.-V. H., Papovich, C., Saintonge, A., et al. 2010, ApJL, 719, L126
Tremblay, G. R., O'Dea, C. P., Baum, S. A., et al. 2015, MNRAS, 451, 3768
Valentino, F., Daddi, E., Strazzullo, V., et al. 2015, ApJ, 801, 132
van der Burg, R. F. J., Muzzin, A., Hoekstra, H., et al. 2014, A&A, 561, A79
Venemans, B. P., Röttgering, H. J. A., Miley, G. K., et al. 2007, A&A, 461, 823
Voit, G. M., & Donahue, M. 2015, ApJL, 799, L1
Wilman, R. J., Edge, A. C., & Swinbank, A. M. 2006, MNRAS, 371, 93
Yuan, T., Nanayakkara, T., Kacprzak, G. G., et al. 2014, ApJL, 795, L20
Zibetti, S., White, S. D. M., Schneider, D. P., & Brinkmann, J. 2005, MNRAS, 358, 949